To the Graduate Council:

I am submitting herewith a thesis written by Raymond P. Young, Jr. entitled "Penetration Mechanisms: An Investigation of the Penetration of Projectiles Impacting Finite-Sized Targets." I have examined the final copy of this thesis for form and content and recommend that it be accepted in partial fulfillment of the requirements for the degree of Master of Science, with a major in Mechanical Engineering.

Roger Crawford

Roger A. Crawford, Major Professor

We have read this thesis
and recommend its acceptance:

Roy J. Schulz

Carroll E. Peters

Accepted for the Council:

CW Minkel

Vice Provost
and Dean of the Graduate School

STATEMENT OF PERMISSION TO USE

In presenting this thesis in partial fulfillment of the requirements for a Master's degree at The University of Tennessee, Knoxville, I agree that the Library shall make it available to borrowers under the rules of the Library. Brief quotations from this thesis are allowable without special permission, provided that accurate acknowledgment of the source is made.

Permission for extensive quotation from or reproduction of this thesis may be granted by my major professor, or in his absence, by the Head of Interlibrary Services when, in the opinion of either, the proposed use of the material is for scholarly purposes. Any copying or use of the material in this thesis for financial gain shall not be allowed without my written permission.

Signature Raymond P. Young, Jr.

Date Nov. 22, 1991

PENETRATION MECHANISMS: AN INVESTIGATION OF THE PENETRATION OF PROJECTILES IMPACTING FINITE-SIZED TARGETS

A Thesis

Presented for the

Master of Science

Degree

The University of Tennessee, Knoxville

Raymond P. Young, Jr.

December 1991

ABSTRACT

Predicting penetration effectiveness of high speed fragments/projectiles is a very difficult task. Empirical, analytical, and numerical hydrodynamic methods are all used to make penetration predictions; however, these methods are limited in usefulness, and should only be used for estimation purposes and not for precise answers.

To obtain valid predictions of projectile penetration, a detailed understanding of the penetration mechanisms is required, along with an understanding of the factors that influence the penetration process.

The current investigation includes the evaluation of selected empirical and semi-theoretical impact models. Normal impacts of chunky ($L/D \simeq 3$) lead projectiles into finite targets were conducted to verify impact theory and evaluate several factors that influence the penetration process. Factors that are found to influence the penetration process include the shape of the penetrator, as well as the density and the dynamic strength properties of the projectile and target materials. Implications about long-rod penetration and material strength effects of targets at very high impact velocities are also presented.

TABLE OF CONTENTS

LIST OF FIGURES

FIGURE		PAGE

FIGURE | PAGE

LIST OF TABLES

NOMENCLATURE

a,b,c,d,k	Constants
BHN	Brinell Hardness Number
C	Speed of sound propagation in material
D	Projectile diameter
E	Internal energy
F	Force
I	Impulse momentum
KE	Kinetic Energy
L	Projectile length
l	Residual penetrator length
m	Mass
P	Penetration depth
p	Pressure
R	Dynamic strength of target material
S	Static shear strength
s	Stagnation point
T	Penetration time
U	Penetration velocity
u	Instantaneous penetration velocity
V	Initial impact velocity
v	Instantaneous residual velocity
VOL	Volume
W	Work

Y	Dynamic strength of the projectile material
ρ	Density

Subscripts

c	Crater
f	Final
i	Initial
p	Projectile
t	Target

CHAPTER I

INTRODUCTION

Over the years, technology has overcome many obstacles, and paved the way for man and machine to reach heights and speeds that were unimaginable just a few decades ago. These new regimes of height and speed, however, are not free of danger, and have provided insight about new forms of weapons and the need for protection against such weapons. This requires an understanding of the laws of nature as they apply to objects that collide at extremely high velocities. A better understanding of such events will aid in the prediction of high-velocity impact damage and the prevention of such damage. This knowledge will also provide a means to assess the damage mechanism, and perhaps the mass and velocity, of meteoroids impacting space systems or debris generated from high energy explosions. Safety problems involving the containment of high-mass or high-velocity fragments or projectiles include the design of nuclear-reactor containment vessels, the transportation of hazardous materials, and the design of armor against hypervelocity weapons.

The study of hypervelocity impacts has been conducted during the past few decades with a varying degree of urgency and excitement [1].[1] It is the purpose of this work to better define the penetration

[1]The numbers in brackets refer to similarly numbered references in the List of References.

mechanisms for a variety of impact events, thus to provide a better understanding of the target/projectile interaction that occurs during impacts in which the materials of projectile and target differ.

During this study, a number of tests were conducted using lead and lead-core projectiles (L/D $\simeq$ 3) impacting wax, Celotex®, lead, and aluminum targets. Impact velocities were varied from 0.22 to 1.24 Km/sec using powder guns. Penetration depths with respect to impact velocity are shown to be characteristic of similar impact tests conducted using dissimilar materials. Impacts were also conducted using projectiles of various construction to evaluate projectile design effects on penetration.

Conclusions about the penetration characteristics of long-rod penetrators and target strength effects at extremely high impact velocities are also presented.

CHAPTER II

PENETRATION MECHANISMS

The term "hypervelocity impact" is currently used to describe regimes of impacts in which particular phenomena occur. Originally, absolute velocities were used to define the hypervelocity impact regime; however, the more recent definition of "hypervelocity impact" to gain favor in the technical community is the impact velocity at which pressures and stresses generated during the impact greatly exceed the strength properties of the projectile and target materials. This definition has gained favor because it allows a significant simplification of the analysis of such impacts. If the projectile and local target materials may be considered fluid, the principles of fluid mechanics may be used as a starting point for hypervelocity impact analysis. This region is also referred to as the "fluid-impact" regime [2]. The impact velocity at which material strengths become negligible varies widely with various projectile and target material combinations. Materials in the liquid state can produce the hypervelocity phenomena at extremely low velocities. Velocities below 1 Km/sec will produce such phenomena in wax targets impacted by wax projectiles. Velocities of 1.5 to 2.5 Km/sec can produce hypervelocity impacts in soft metals such as lead, tin, gold, and indium. Velocities of 5 to 6 Km/sec must be achieved before hypervelocity phenomena can be triggered in typical structural and stony materials such as aluminum, steel, quartz, and so on. Finally, velocities of 8 to 10 Km/sec and above are required to produce the phenomena in very strong materials such as berylium and boron metals, hard ceramics like alumina or boron carbide, and finally diamond [1].

The universally accepted characteristic of craters produced in the hypervelocity impact regime by "chunky" projectiles (all dimensions comparable) is that the crater produced has a hemispherical shape and penetration is approximately one-half the crater diameter at the original surface of the target. Obviously, the ultimate "chunky" projectile is the sphere, but cubes, cylinders with length to diameters ratios (L/D) less that three, blunt cones and so forth, all meet this criterion and produce craters of similar shape when impacts are in the hypervelocity regime [1].

During the early 1960's, extensive analytical and experimental programs were conducted to develop an understanding of the penetration processes. During that period, a phenomenological model of the hypervelocity impact event was formulated by the technical community [3]. The mechanics of the penetration process can be described in terms of four phases. The four phases consist of the 1) "transient", 2) "steady-state" penetration, 3) "cavitation", and 4) "recovery" phases. It should be noted that all four impact phases may not occur or contribute to the final crater dimensions for all impact events.

Transient Phase

The first stage of the penetration process to occur during an impact event is referred to as the transient phase. This phase occurs immediately upon contact of the projectile and the target. At the onset of the impact, compressive stress waves are generated in both the projectile and target. The stress waves are considered to be one-dimensional since relief waves from free surfaces and material interfaces have not had time to act. Shock waves are generated in the target and projectile that can travel at velocities greater than the speed of sound in the respective materials. Factors governing material response in this phase are the density and compressibility of local material elements in the projectile and target in the vicinity of the impact interface [4].

In the hypervelocity impact regime, the stresses are much greater than the mechanical strength of either the projectile or target. For example, a steel sphere impacting a lead target at 6.0 Km/sec will produce impact pressures in the steel greater than 206.8 GPa during the transient phase [2]. This pressure is more than one hundred times the ultimate strength of steel. Under such conditions the materials are believed to behave as fluids with virtually no strength at all [2].

The transient phase of the impact process is extremely short in duration and may be as brief as a nanosecond for blunt faced projectiles or up to as long as required for a sphere to penetrate the target approximately one diameter [4]. Figure 1[2] (which should be interpreted on a qualitative basis only, since the absolute values of pressure and time are functions of the impact parameters) represents a typical pressure history generated at the interface between the projectile and target throughout an impact event [5].

---

[2]Figure 1 and all subsequent figures are contained in Appendix A.

The propagation rate of the compressive stress waves, along the impact axis, will be at either the speed of sound of the materials making up the target and projectile for subsonic impacts or at the penetration velocity for hypersonic impacts. The stress wave propagation in the radial direction will be at the speed of sound of the target and projectile materials, respectively.

Steady-State Penetration Phase

The second phase of the impact process is the "steady-state" penetration phase. It is during this phase of penetration that the projectile dissipates its kinetic energy. The densities, compressibilities and other mechanical properties of the projectile and target materials all enter into the determination of the intensity and duration of the pressure pulse produced in the target. Projectile shape will also influence the duration of the steady-state penetration phase. Low-aspect-ratio projectiles (i.e., thin disks) will produce relatively short duration steady-state phases, while high-aspect-ratio projectiles (i.e., long rods), will produce relatively long steady-state penetration phases during impacts that occur in the "hypervelocity impact" regime [3, 5]. The pressure in the deforming region of the projectile will vary from point to point, but may be roughly estimated as [1]

$$P > 1/2\, \rho_p V_p^2. \tag{1}$$

During low-velocity impacts, impacts in which pressures generated do not greatly exceed the material yield strengths of the projectile and target, material mechanical properties such as strength and ductility greatly influence the impact dynamics, and the resulting crater. Projectiles made of soft, low dynamic strength materials will not penetrate targets made of relatively strong materials at low velocities and simply flatten on the surface of the target. Penetration will not occur until the pressures generated during the impact exceed the target dynamic yield strength. As impact velocities increase, penetration begins to occur, and the resulting crater is generally shallow and broad. As the impact velocity continues to increase, the projectile will deform as it penetrates resulting in a crater that resembles a vase. As impact velocities continue to increase into the "hypervelocity impact" regime, the cavitation phase begins to influence the final crater shape.

Impacts between relatively strong projectiles and weak targets produce significantly different impact craters. At low impact velocities, the impact pressures generated are not great enough to deform the projectile, and the crater produced is a deep, narrow cavity. The penetration depth increases steadily with the 4/3 power of the velocity for metal target and projectile combinations; that is, doubling the velocity increases the penetration depth by a factor of about 2.5. This relationship holds for a number of different materials, and is used in many of the classic impact formulas [2]. As the impact velocities are increased, pressures increase to values that produce plastic deformation and/or break-up of the projectile. Ductile projectiles tend to mushroom and begin to turn inside out. The crater becomes larger in diameter and the penetration depth decreases because the projectile deforms as impact velocities are increased. As impact velocities are continually increased, and the projectiles continue to deform and break-up into finer pieces, the penetration depth continues to fall and finally starts to increase again, however, at a much lower rate. This marks the onset of the next stage of the penetration process known as the cavitation phase.

Projectiles and targets made of the same materials, or materials having similar strength properties, demonstrate a third cratering process. At any impact velocity at which pressures are generated above the dynamic strength, both the projectile and target begin to deform. A ductile projectile will mushroom, and as impact velocities continue to increase, the projectile will turn inside out. A brittle projectile/target combination will fracture as the penetration proceeds until the projectile has completely eroded. At velocities above the point at which the projectile has either eroded or turned itself inside out, the cavitation phase continues the penetration process.

Cavitation Phase

In this phase of the impact mechanism, the crater begins to widen and approach the characteristic hemispherical shape indicating the beginning of the "hypervelocity impact" regime [2]. This phase generally begins after the projectile has been completely deformed or eroded and essentially removed from the system as a continuing source of energy. After the projectile has been completely eroded or deformed, the crater may continue to expand as a result of the momentum that has been transferred from the projectile to the target material. This phase continues until the energy density behind the shock wave becomes too small to overcome the strength of the target material. At this point the shock wave has been reduced to an elastic or plastic wave which continues to travel into the target until the trapped energy has been dissipated [4].

As the velocity of a projectile is increased, an increasing portion of the projectile's kinetic energy is exhausted in widening the crater rather than increasing the penetration. Eventually the crater becomes almost exactly hemispherical. As the impact velocity is further increased, the hemispherical crater expands radially and hence in depth. The penetration in this phase of an impact tends to vary with the 2/3 power of velocity for many target materials. That is, doubling the velocity increases the penetration by a factor of about 1.6 [2].

Ductile projectiles tend to flow over the crater surface and remain as a thin plating. The small particles of brittle projectiles that have been shattered will also flow out over the surface of the crater [2].

Recovery Phase

The final phase of the impact mechanism is the "recovery phase". It is in this phase that the stress waves have been attenuated to levels that no longer cause plastic deformations of the target, and elastic recovery of the target material occurs. This phase may also include brittle-type fracture of the crater surface, and recrystallization and annealing beneath the crater surface.

Although the above model of the penetration process is presented as four distinct phases, the complete process of the crater formation is actually without discontinuities. In other words, the different phases of the impact process can occur simultaneously.

The characteristics described above lead to interesting target penetration results. Crater characteristics and penetration depths as a function of impact velocity are shown schematically in Figures 2 and 3, respectively. Figure 3 characterizes the three impact scenario of; 1) relatively weak projectiles impacting strong target materials, 2) strong projectiles impacting relatively weak target materials, and 3) impacts of projectiles and targets with similar material properties. The penetration of relatively strong projectiles into weak targets tends to be a strong function of velocity in the low-velocity regime where the projectile remains rigid. Projectile deformation (mushrooming) is marked by a reduction in the penetration effectiveness as impact velocities continue to increase into the projectile-pulverization regime. The penetration effectiveness again increases as the "hypervelocity impact" regime is reached. Weak-projectile impacts into strong targets produce craters whose depths increase slowly with impact velocity at relatively low impact velocities, and then increase to a 2/3-power velocity dependence as the "hypervelocity impact" regime is approached. Target-projectile combinations with material properties and design strengths between these two extremes display intermediate behavior, although they all share the common characteristics [1, 6].

It has been shown through impact experiments that ductile materials flow for significantly longer times after impact than do brittle materials, apparently because of the decrease in the resistance to deformation at extremely high strain rates. This behavior is not clearly understood, but is similar to that observed in some impact-extrusion processes. The brittle materials tend to increase in resistance to deformation with increasing strain rates, even at the extremely high strain rates involved in hypervelocity impacts. These peculiarities of ductile and brittle materials have been one of the main sources of difficulty in formulating a complete impact phenomenology [7].

CHAPTER III

THEORETICAL IMPACT MODELS

Solutions to impact problems have taken one of three separate forms. The most common is the empirical approach, where large amounts of data are obtained and correlated. This is a useful means to solve specific problems; however, extrapolation of the information obtained to other materials, geometries, or velocities outside the range of the test is difficult and may be invalid.

A second method used in attempting to solve impact problems is the development and use of engineering models. These models are usually based on the combined application of the fundamental conservation laws and assumptions pertaining to the deformation and failure processes gained from prior observations. This approach can range anywhere in sophistication from a simple one-dimensional penetration model to more complex two- and three-dimensional models based on combinations of mechanisms and assumptions. It is sometimes hard to distinguish the first two approaches in literature because of the overlapping methods sometimes used. Many empirical observations and curve-fitting schemes are referred to as models.

The third approach to solving impact problems is a method that divides the target and projectile into small elements and applies the fundamental laws of physics to each element. This is a very complex method and can only be applied to one problem at a time. The numerical procedure must be reapplied each time there is a change in the input variables. Dynamic material properties, of both the projectile and the target, must be well established for all combinations of strain, strain rate, temperature, and loading history. While properties are partially defined for some of the more common materials, data bases are very incomplete for most materials. Computational results are generally compared to test results, and input variables are modified to force the calculation to match the test result. Therefore, the computations are correlative rather than predictive.

Each of the three procedures for solving impact problems has its merits and disadvantages. Because one or two of these procedures cannot always provide the desired information concerning the impact phenomenon, a combination of all three procedures is often the best approach [4].

Because there is no single theoretical approach that can fully describe the impact process, only an overview of some of the more common methods used to predict projectile penetration will be presented.

Analytic Models

Nearly all of the work done in impact dynamics, ballistic modeling, and numerical simulation of impact events is based on the three fundamental conservation laws; conservation of mass, momentum, and energy. The conservation of mass simply states that mass is conserved on a physical system,

$$\int_{VOL} \rho \, d\,VOL = Constant \qquad (2)$$

where ρ is the mass density (mass per unit volume) and VOL is the volume of the body.

The conservation of momentum can be expressed or applied in several ways. It is a statement of Newton's second law,

$$F = m\,dV/dt. \qquad (3)$$

For a closed system of n masses, m_j, not acted upon by any external forces, the conservation of momentum states,

$$\sum_{j=1}^{n} m_j V_j = Constant. \qquad (4)$$

The impulse-momentum law is obtained by multiplying (3) by dt and integrating,

$$I = \int F\,dt = \int m\,dV = mV_f - mV_i \qquad (5)$$

which states that the impulse, I, imparted to a body changes the momentum from an initial value, mV_i, to a final value, mV_f, where V is velocity.

The conservation of energy is written in a form where the system being considered is a set of j discrete masses or volumes. Denoting the initial state by the subscript i and the final state by the subscript f, The conservation of energy requires,

$$\sum_j E_i + \sum_j 1/2\,\rho\,V_i^2 = \sum_j E_f + \sum_j 1/2\,\rho\,V_f^2 + W \qquad (6)$$

where E is the stored (elastic) internal energy and W represents work done on the system.

Bernoulli's equation has been used to model very high velocity impacts in which the high pressures generated cause the projectile and target materials to behave essentially as inviscid fluids. For the high velocity application, the Bernoulli equation states that the change in kinetic energy of a fluid under steady-state flow conditions equals the work done on the fluid. In this case, the work is produced by the differential pressure acting on the volume (or density) in going from one state to another.

$$p_i + 1/2\,\rho_i\,V_i^2 = p_f + 1/2\,\rho_f\,V_f^2 \qquad (7)$$

where p is the pressure, ρ is the density, and V is the velocity.

The simplest analytical equation used for the prediction of projectile penetration is the fluid jet equation, also referred to as the "Munroe Jet" equation developed in 1885 [4]. This approach assumes that projectile penetration in the hypervelocity-impact regime and shaped-charge jet penetration are the same physical phenomenon. As such, the study of the hypervelocity impact is an extremely attractive starting point for developing a quantitative understanding of more generalized impact processes. The geometric definition of the long rod penetrator is that the L/D is much greater than 1. The penetration theory of the rod penetrator is started with the theoretical basis of the shaped-charge jet or fluid-jet penetration model. Figure 4 represents the penetration behavior of a rod or fluid jet of length L and density, ρ_p, impacting a semi-infinite target of density ρ_t with a velocity V_p. In the hypervelocity impact regime, the material-strength influences are considered negligible, and the rod is regarded as penetrating like a fluid jet. The penetration behaves as a steady-state flow with dynamic flow pressure equilibrium at the stagnation point, s, between the rod and target material [4]. From the stagnation point, the rod material flows radially and the projectile forms a hollow tube inside the crater. The stagnation point moves at velocity, U_p, while the end of the projectile continues to travel at the initial impact speed. Stress waves traveling in both the rod and target are neglected. Because $V_p > U_p$, the instantaneous length l decreases permanently and the erosion rate becomes

$$dl/dt = -(V_p - U_p). \tag{8}$$

For steady-state flow, neglecting material compressibility and considering only one-dimensional flow, the Bernoulli equation becomes,

$$1/2\, \rho_p \left(V_p - U_p \right)^2 = 1/2\, \rho_t U_p^2 = Constant \tag{9}$$

for pressure equilibrium at the stagnation point. A constant penetration velocity can be obtained using Equation (9).

$$U_p = V_p / (1 + (\rho_t/\rho_p)^{1/2}) \tag{10}$$

The penetration is assumed to stop when the projectile is completely eroded. Therefore. the penetration time, T, can be calculated by integrating Equation (8),

$$T = L / (V_p - U_p). \tag{11}$$

The penetration depth can now be expressed as

$$P = U_p * T \tag{12}$$

From Equations (9), (10), and (12) the penetration formula for a fluid jet is obtained

$$P = L\left(\rho_p/\rho_t\right)^{1/2} \tag{13}$$

This equation is a function of the material densities only, and assumes that the hypervelocity impact regime has been reached; therefore, this equation can only be expected to be valid only at high impact velocities.

Deficiencies in this mathematical model are readily seen in comparison with impact data. Material strengths and impact velocities play strong roles in the penetration dynamics as described earlier. This model also ignores the cavitation and recovery phases of the impact process.

Because of the deficiencies of the fluid-jet penetration equation, Allen and Rodgers [4] attempted to explain the differences between theory and experimental data by introducing an additional term into the Bernoulli equation. The new term, represented by R', is described as the difference in the "dynamic strengths" of the target and projectile material.

$$R' = R - Y \tag{14}$$

where Y and R are the dynamic strengths of the projectile and the target material, respectively. The dynamic strength of a material infers a material strength quantity at various strain rates. For most empirical data, the "dynamic strength" values required to fit the data have no physical significance. Including the value of R', the Bernoulli equation becomes

$$1/2\,\rho_p\left(V_p - U_p\right)^2 = 1/2\,\rho_t\,U_p^2 + R' = Constant. \tag{15}$$

For values of R = Y, this equation is no more valid than Equation (9). For R' = 0, penetration occurs (Up > 0) if Vp > 0, and there will be no penetration at projectile velocities at which the dynamic flow pressure does not achieve R'.

$$U_p = 0,\;\; 1/2\,\rho_p\,V_p^2 \le R' \tag{16}$$

When the dynamic pressure exceeds R', penetration begins to occur.

$$U_p > 0,\ 1/2\,\rho_p V_p^2 > R' \tag{17}$$

From Equations (16) and (17), a velocity limit at which penetration will occur can be expressed as

$$V_{lim} = \left(\frac{2R'}{\rho_p}\right)^{1/2} . \tag{18}$$

Figure 5 represents a typical impact curve generated using the Allen and Rodger's equation for impacts that occur for values of R' > 0. Also plotted for comparison is the fluid-jet equation. The penetration depth normalized by the projectile length has been termed the penetration efficiency or penetration effectiveness.

Solving Equation (15) for U_p, the penetration velocity becomes

$$U_p = \frac{\rho_p V_p - \left[\rho_p^2 V_p^2 - 2\left(\rho_p - \rho_t\right)\left(1/2\,\rho_p V_p^2 - R'\right)\right]^{1/2}}{\rho_p - \rho_t} . \tag{19}$$

Using Equations (19), (11), and (12), the penetration depth is given by

$$P = L\,\frac{-\rho_p V_p + \left[\rho_p^2 V_p^2 - 2\left(\rho_p - \rho_t\right)\left(1/2\,\rho_p V_p^2 - R'\right)\right]^{1/2}}{\rho_t V_p - \left[\rho_p^2 V_p^2 - 2\left(\rho_p - \rho_t\right)\left(1/2\,\rho_p V_p^2 - R'\right)\right]^{1/2}} . \tag{20}$$

For the special case of $\rho p = \rho t = \rho$, Equations (19) and (20) simplify to

$$U_p = \frac{V_p}{2}\left(1 - \frac{2R'}{\rho V_p^2}\right) \tag{21}$$

and

$$P = L\,\frac{\left[1 - \left(2R'/\rho\,V_p^2\right)\right]}{\left[1 + \left(2R'/\rho\,V_p^2\right)\right]}\,. \tag{22}$$

The Allen and Rodgers equation produces a variation of the penetration depth with velocity; however, the penetration of the projectile approaches the fluid-jet equation at high velocities (1/2 ρ_p V_p^2 >> R'), again neglecting the cavitation and recovery phases of the impact process [4].

The Tate and Alekseekii model [4] is based on a knowledge about elastoplastic wave propagation in a rod. This model was developed to include the rod length and velocity reduction throughout the impact process. Again, the Bernoulli equation was modified to reconcile the the impact velocity (Vp), each instantaneous residual velocity (v), and the corresponding instantaneous penetration velocity (u) [4]. And terms are included in the Bernoulli equation, Y and R, for the dynamic strengths of the projectile and target material respectively.

$$Y + 1/2\,\rho_p (v - u)^2 = 1/2\,\rho_t\,u^2 + R \tag{23}$$

From Equation (23), the following instantaneous penetration velocities are obtained.

$$u = \frac{v - \mu\,(v^2 + A)^{1/2}}{1 - \mu} \tag{24}$$

where

$$\mu = \left(\rho_t/\rho_p\right)^{1/2} \tag{25}$$

and

$$A = \frac{2\,(R - Y)(1 - \mu^2)}{\rho_t}. \tag{26}$$

Accounting for the deceleration of the residual rod during penetration, neglecting the plastic wave propagation and applying Newton's law in the following form, one obtains:

$$Y = -\,\rho_p\,\ell\, dv/dt. \tag{27}$$

The erosion rate is given by:

$$d\ell/dt = -\,(v - u). \tag{28}$$

It follows that:

$$d\ell/\ell = \frac{\rho_p\,(v - u)}{Y}\,dv. \tag{29}$$

Insertion of Equations (24), (25), and (26) into (29), followed by integration, gives the relationship between the instantaneous rod length and the instantaneous rod velocity.

$$\ell/L = \left[\frac{v + (v^2 + A)^{1/2}}{V_p + (V_p^2 + A)^{1/2}}\right]^{\left(\frac{R-Y}{\mu Y}\right)} exp\left(\frac{\mu\rho_p}{2(1-\mu^2)Y}\left\{\left[v\,(v^2 + A)^{1/2} - \mu v^2\right] - \left[V_p\left(V_p^2 + A\right)^{1/2} - \mu\,V_p^2\right]\right\}\right). \tag{30}$$

This equation has been solved for a variety of cases in which the dynamic strengths of the target and projectile materials have been varied to show the influence of material dynamic strength on the impact penetration phenomena. For this study, the results of the penetration model are of interest and a more detailed solution of Equation (30) can be found in References [1], [4], [8], and [9]. Simplified cases are plotted in Figure 6 that demonstrate the effect of material dynamic strengths of the target and projectile on penetration when the densities of the two materials are equal. Unfortunately, it is not clear what dynamic strength values should be used in these equations, because the dynamic strengths of the materials are generally expected to be a function of the local strain rate [3].

The fluid jet equation is again presented in Figure 6 and demonstrates that at the high velocities the Tate and Alekeevskii equation also converges to $(\rho_p/\rho_t)^{1/2}$. Again, the cavitation and recovery phases of the impact process have not been modeled. The Tate and Alekseevskii equation does, however, describe impact characteristics that are produced for low velocity impacts of materials of varying strength. Several experiments have been conducted and used as proof of the existence of a maximum penetration value, including the data obtained by Tate in 1969 and shown in Figure 7. This data pertain to aluminum-alloy rods with an L/D of 10 impacting into semi-infinite lead targets. The calculated curve fits the data well for values of Y = 1.52 GPa for the aluminum-alloy and R = 0.36 GPa for the lead materials. The ultimate yield strengths for these materials under static conditions are 0.18 and .0128 GPa for aluminum-alloy and lead, respectively [10, 11]. The very high values of R and Y required to fit the data as compared to the respective static strengths are explained by the pronounced strain-rate effects on the dynamic strength of a material [4]. Values of R and Y must be obtained experimentally at the strain rates produced by the impacts.

The data presented in Figure 7 were obtained at relatively low impact velocities compared to those achievable today. It should also be noted that the "hypervelocity impact" regime has not been reached for aluminum at impact velocities of 2.5 Km/s. As stated earlier, impact velocities of 5.0 to 6.0 Km/s are required to trigger the "hypervelocity" response in aluminum. Impacts are required at much higher velocities to prove the existence of a maximum penetration efficiency (P/L) for the projectile/target designs and materials of this experiment.

Empirical Models

Today, as in the past, most of the work done in penetration mechanics is experimental in nature. Efforts to fit experimental observations empirically with selected parameters (such as Brinell Hardness Numbers, speeds of sound in the target/projectile materials and material strengths) have been conducted for many years. The experimental approach has several advantages, and several limitations. The prime advantage is that, in many impact events, experimentation is the only means of obtaining answers to complex problems. The major disadvantage is that the empirical relations developed apply only to a particular range of parameters included in the original experiments.

Empirical methods also serve to collate the data and provide some clues to the physical phenomena of impact dynamics. Care must be taken to not extrapolate beyond the range of the database, since this can provide predicted results that are in considerable error.

The selected empirical models presented in this section are based on studies of penetration into semi-infinite targets, and by no means include all of the empirical studies or models developed. They are, however, a good cross-section of the various empirical penetration models that have been developed.

Most of the work conducted in the study of the penetration phenomena is concerned with the determination of crater depth and volume created by impacts of kinetic energy projectiles. Other work done in the field is concerned with the amount of residual projectile remaining in the crater after a relatively low velocity impact [4]. Several empirical formulas have been developed that represent the experimental measurements fairly well over restricted regions [2].

Many of the models for hypervelocity impacts show characteristics similar to an equation proposed by Christman and Gehring in 1966. This impact model was developed for impact velocities between 2.0 and 6.7 Km/sec and includes the penetration effects of the steady-state penetration and cavitation phases [5]. The dimensionless penetration equation for semi-infinite metal targets is expressed as

$$P/L = \left(1 - \frac{D}{L}\right)\left(\frac{\rho_p}{\rho_t}\right)^{1/2} + 2.42\, D/L \left(\frac{\rho_p}{\rho_t}\right)^{2/3}\left(\frac{\rho_t V_p^2}{BHN}\right)^{1/3}. \tag{31}$$

The first term of Equation (31) represents the steady-state penetration phase of the impact. The effective length of the penetrator in the steady-state penetration phase is reduced by one rod diameter. The remaining diameter of rod length is assumed to contribute to the cavitation phase of penetration as represented by the remaining empirical term. The second term, used to account for the additional penetration experienced during the cavitation phase, was required to fit impact data that exceeded the penetration predictions calculated using the fluid-jet equation.

A second impact penetration model was proposed by Swift [1] for chunky projectiles in the hypervelocity regime. This model is based on the assumption that the crater volume, VOLc, is proportional to the kinetic energy, KE, of the projectile.

$$VOL_c = k\,(KE)_p \tag{32}$$

Values of the proportionality, k, constant are dependent on the dynamic strength properties of both the projectile and target. The value for the constant, k, has to be derived experimentally at the different impact energies, and is usually in the range of 0.5 to 2.0E+03 J/cm^3. Equation (32) can be expanded by evaluating the crater volume as hemispherical (impacts occurring in the hypervelocity impact regime) and by assuming the crater volume is proportional to the projectile kinetic energy. This produces the relationship

$$P/L = \left(\frac{\rho_p k}{4}\right)^{1/3} V_p^{2/3}. \tag{33}$$

Equation (33) provides the relationship that has been observed in many hypervelocity impact experiments, that is the penetration depth varies with the 2/3 power of the impact velocity. Equation (33) also yields the relationship that the size of the crater scales linearly with projectile dimensions. This scaling dependence has been investigated carefully and found to be nearly correct; however, the crater size has been found to increase with the projectile diameter to the 0.06 power [1].

$$P/L = \left(\frac{\rho_p k}{4}\right)^{1/3} D^{.06}\, V^{2/3} \tag{34}$$

and

$$VOL_c = k\,(KE)_p\, D^{.12} \tag{35}$$

Again, this expression for penetration was derived for chunky projectiles (L $\simeq$ D) in the "Hypervelocity Impact" regime. The behavior described by Equation (34) is shown in Figure 8, and is similar to results obtained experimentally. The small deviation from linear size-scaling dependence is unimportant when scaling by factors of up to 1:10, however, it can become important when scaling between micro and macro impacts [1].

In addition to the above impact models, the following expressions are presented here to illustrate the possible importance of other physical parameters.

The Charters and Summers, or Ames, criterion in the form

$$P/L = 2.25 \left(\frac{\rho_p}{\rho_t} \frac{V_p}{C_t} \right)^{2/3} \tag{36}$$

was chosen for the strong dependence on target and projectile densities [12]. This density dependence can be seen in most of the impact models developed and will generally be in terms of the density ratio to the 1/2, 2/3, or 1/3 power.

The Herrmann and Jones law [4] in the form

$$P/L = 0.6 \left(\frac{\rho_p}{\rho_t} \right)^{2/3} \ell n \left\{ 1 + \frac{100}{4} \left(\frac{\rho_p}{\rho_t} \right)^{2/3} \frac{\rho_t V_p^2}{BHN} \right\} \tag{37}$$

represents an empirical correlation for a large number of projectile/target combinations. The densities are expressed in gm/cm^3, the projectile velocity is expressed in Km/sec, and the Brinell Hardness Number is expressed in terms of Kg/mm^2.

The Gehring and Eichelberger [4] equation is a model that assumes the impact crater is hemispherical and directly proportional to the energy regardless of the projectile.

$$P/L = \left(\frac{5 \rho_p V_p^2}{BHN} \right)^{1/3} \tag{38}$$

The density, velocity and Brinell-Hardness-Number terms are expressed in the same units as the Herrmann and Jones equation.

Another expression that has been used to correlate a large number of projectile/target material combinations is the Sorensen equation:

$$P/L = 0.311 \left(\frac{\rho_p}{\rho_t} \right)^{0.167} \left(\frac{\rho_p V_p^2}{S_t} \right)^{0.282} \tag{39}$$

The target static shear strength, S_t, is expressed in terms of dynes/ cm^2, density in terms of gm/cm^3, and projectile velocity in terms of cm/sec. This correlation also assumes the impact craters are hemispherical and that both the target and projectile are metals [4].

The last empirical model to be presented in this study is the that of Johnson and Walsh [4]. This correlation was derived from hydrocodes and then compared to test data. The following equation was obtained.

$$P/L = k \left(\frac{\rho_p}{\rho_t} \right)^{1/3} \left(\frac{V_p}{C_t} \right) \tag{40}$$

The constant, k, is a term obtained from experimental correlations and depends on the strength of the target/projectile combination. This correlation is limited to impacts in which: 1) the impact velocity is greater than 1-2 times the speed of sound in the target material, 2) the projectile aspect ratio is within a factor of three of unity, and 3) the projectile density is within a factor of about 3 of the target density [13].

Some of the above correlations are presented and compared to selected data of the present study in the following chapters. Although a vast amount of experimental data has been obtained, no completely adequate empirical or theoretical model has been formulated. Most empirical models are rules-of-thumb that aid in the design of test programs but can not be considered to yield quantitive results accurate enough for most engineering purposes.

CHAPTER IV

EXPERIMENTAL STUDY

The purpose of the present investigation was to develop an empirical equation for the impact phenomena of "chunky" projectiles into targets of various materials. Target materials chosen were 6061-T6 Aluminum, bee's wax, Celotex®, and lead. These target materials represent a wide range of strengths and densities (see Table 1)[3]. The projectile material chosen was lead. Target and projectile materials were also chosen because the hypervelocity impact phenomena can be achieved for most of these materials at relatively low impact velocities. Lead projectiles and targets have also been used in past studies at relatively low impact velocities to simulate other much-stronger dense materials impacting at much higher velocities.

The data were obtained in the velocity range of 0.22 to 1.24 Km/sec using single-stage powder guns and "off-the-shelf" ammunition. The front surface of the targets were placed normal to the projectile trajectory, and approximately 4 cm from the muzzle of the gun to minimize projectile velocity decay caused by aerodynamic drag. Projectile velocities were obtained from manufacturers' specifications of the ammunition and verified using other references. Projectile velocities using off-the-shelf ammunition will vary depending on the length and dimensions of the gun barrel used, the chambering action of

---

[3]Table 1 and all subsequent tables are contained an Appendix B.

the gun, and variances from one ammunition lot to the next. Efforts were taken to minimize the effects of the above gun/ammunition uncertainties. Guns were chosen to have barrel length as those used to test the ammunition by the manufacturer. Guns used include the following: 1) a Mossberg Model 124-A (cal. .22, bolt action), 2) a Browning Model BL-22 (cal. .22, Lever action), 3) a Revelation Model 107 (cal. .22 Magnmum, bolt action), 4) a Remington Model 788 (cal. .223 Remington, bolt action), and 5) a Springfield Model 1903-A3 (cal. 30-06, bolt action). Specifications for most of the ammunition used in this study quoted the projectile velocity to be accurate within approximately $\pm$ 0.009 Km/sec. Data shots were repeated a number of times to account for velocity uncertainties of the ammunition, and data scatter is represented as error bars on the plotted data. A total of 218 shots were made. A description of the projectiles/ammunition used for this study are given in Table 2. Projectile velocities presented in Table 2 are quoted from References [14], [15] and [16]. Penetration data were also compared between impacts conducted using ammunition with similar specifications from more than one manufacturer, and no significant differences in the penetration data were observed. Generalized projectile configurations are shown in Figure 9. The higher velocity projectiles (V_p > 0.58 Km/sec) were manufactured with thin copper-alloy jackets around the lead-alloy cores. The high velocity impact tests into Celotex were conducted using jacketed and modified projectiles. Projectile modifications were made by removing the thin copper-alloy jackets from the exposed portion of the projectile (the portion of the projectile concealed by the ammunition cartridge remained intact). This modification resulted in a lead projectile with a small copper-alloy cap on the base. All impact data presented using wax as the target material were obtained using modified projectiles. The thin copper-alloy jackets were not removed when firings were made into the lead or aluminum targets, since the effects of the copper-alloy jackets on the crater formation in these materials can be assumed to be negligible.

All data were obtained at atmospheric conditions, and at a temperature of approximately 76° Fahrenheit.

Data obtained included impact crater and post-test projectile dimensions. Crater depth measurements were made from the undisturbed surface of the target to the deepest part of the crater. Crater volume measurements were obtained by filling the craters with known volumes of water. The crater volume is considered to include only the volume of the crater below the undisturbed surface of the target.

CHAPTER V

DISCUSSION AND RESULTS

Impacts into Lead Targets

Impact tests were conducted on lead projectiles fired into lead targets (10 cm. diam., and 15 cm. thick). The use of similar target and projectile materials simplified the analytical models and most of the empirical models. A target-projectile density ratio of unity simplifies the penetration predictions of most impact models. The fluid-jet model simplifies to P = L (predicted penetration depth is equal to the length of the projectile). As can be seen in the data obtained for this study (Figure 10), the depth of penetration exceeds the fluid-jet model at a velocity of approximately 0.36 Km/sec for the solid projectiles and 0.45 Km/sec for the hollow projectiles. A penetration depth exceeding the predicted penetration depth of the fluid-jet has been observed in most impact testing [4], and has been attributed primarily to the cavitation phase of the impact mechanism. The penetration curve of the solid projectile tends to follow the expected impact trends for projectile-target combinations of similar strength and density materials. However, the penetration curve of the hollow point and flat-nosed projectile is significantly low at the lower velocities and approaches the solid penetrator curve at the higher velocities (> 0.6 Km/sec). This phenomena has been shown to occur in studies by Brooks, Erikson, and Woodward and Wilkins [4, 17, 18]. They demonstrated that the projectile-tip shape can influence the penetration depth at the lower impact velocities. The tip geometry will influence the geometry of the initial plastic flow in the target and projectile, the stress distribution in the target, and possibly the break-up of the projectile. Most of the past studies varied the half-angle of conically tipped rod projectiles. Each of the past studies demonstrated an increased depth in penetration depth at the lower velocities with the sharper pointed projectiles producing the greater depth of penetration. Above a certain critical velocity, the depths of penetration of the different projectiles were essentially identical. Similar results are indicated by Figure 10. The hollow-point and flat-nosed projectiles produced shallower craters at the lower velocities. It should also be noted that the hollow-point projectiles are weaker structurally than solid projectiles. At an impact velocity of approximately 0.6 Km/sec the penetration curves merge. Past studies indicate that the critical velocity corresponds to an impact velocity at which the projectile nose was quickly deformed or removed. It should be noted that only nose tips of about 10% of the body length were varied in past investigations. The projectiles of this study were structurally nonuniform for approximately 30% of the body length. If it is assumed that the variations in the penetration depth of a projectile are a function of how quickly the differences of varying designs are eroded or removed, then the critical impact velocity required for the penetration curves to merge would increase as the relative nose/hollow-point length is increased. At impact velocities below 0.6 Km/sec, the hollow-point projectiles produced wider craters than did the solid projectiles, and also produced a characteristic "tit" at the bottom of each crater (Figure 11). At velocities above 0.6 Km/sec, there were no measurable differences of the impact craters produced by the solid or hollow point projectiles, and the characteristic "tit" of the hollow point projectile was no longer present.

The impact craters produced in this study are characteristic of the classic penetration processes described earlier. The craters were generally narrow at the lower impact velocities and widened to the hemispherical crater characteristic of the hypervelocity impact regime at the highest impact velocities. The projectiles mushroomed, and turned inside out at the higher impact velocities. Projectile pretest surface features were visible on the inverted post-test projectile residue at impact velocities up to 0.4 Km/sec. The projectile had completely inverted at 0.4 Km/sec and the residual projectile material became a thinner coating on the crater surface as the crater began to expand radially with increasing impact velocities. Figure 12 presents the crater volume versus velocity, and Figure 13 presents the projectile residual thickness, along the shot axis, in percent of original projectile length as a function of impact velocity. Note that, at the impact velocity at which the projectile is essentially eroded (turned inside out), the fluid-jet equation is satisfied (P = L). Increasing impact velocities produced craters with thin strips of residual projectile material attached to the crater sides. The projectile material had stretched beyond the plastic limit and begun to tear at an impact velocity of approximately 1.0 km/sec. At an impact velocity of 1.24 Km/sec, the crater shape was characteristic of the classic hypervelocity impact crater. The inverted projectile expanded with the crater, fragmenting into small thin flakes deposited on the crater surface.

Impacts into Celotex® Targets

Impacts of lead projectiles into Celotex targets (15 cm. X 15 cm. X 122 cm. thick) produced penetration curves characteristic of strong projectiles impacting relatively weak targets (see Figure 14) At the lower impact velocities ($0.0 < V_p < 0.4$ Km/sec) penetration was a strong function of impact velocity and nearly linear. The craters produced were long, narrow cavities with diameters equal to the penetrator. The projectiles remained essentially undeformed. The impact velocity regime of non-deforming projectile penetration for the hollow point projectile is slightly smaller, since the projectiles began to deform at approximately 0.36 Km/sec. This phenomenon was expected because of the weaker nose construction of the hollow-point projectile. Projectile mass recovered, expressed in percent of pretest projectile mass, versus impact velocity is presented in Figure 15. Noted that Celotex is rather abrasive, and the surfaces of all projectiles were slightly eroded at the lower impact velocities. Jacketed projectiles were not as subject to erosion in the Celotex target and the mass loss above impact velocities of 0.6 Km/sec was caused primarily by projectile fragmentation after mushrooming. The decrease in penetration efficiency, P/L, with increasing impact velocity is marked by the initiation of gross projectile deformation and/or mass loss. This phenomenon has been reported in other impact tests conducted with relatively strong projectiles impacting relatively soft targets [19].

Below a velocity of 0.36 Km/sec, the penetration curves for the solid and hollow point projectiles are expected to be essentially the same. Post-test examination of the projectiles revealed that the hollow voids of the hollow point projectiles were filled with Celotex early in the impact process. Thus, the hollow-point projectiles behaved essentially as solid projectiles, with the same drag characteristics as the solid-projectile configuration. This observation is supported by the penetration data at a velocity of approximately 0.36 Km/sec, at which the solid and hollow-point penetrations are essentially the same.

As the impact velocities were increased, and the projectiles began to deform (mushroom) and erode, the penetration curves for the hollow-point and solid projectiles began to deviate. The hollow-point projectiles experienced more deformation than did the solid projectiles and consequentially did not penetrate as deeply. The craters produced at the higher impact velocities increased in radius, but were still rather narrow. This variation in penetration depth continues until the impact velocity is such that the differences in the projectile design are eroded away early in the impact, and the penetrations continue with projectile residues of essentially the same shape. The penetration curves merge at a velocity of approximately 1.2 Km/sec. The projectile residues of the different projectiles at this velocity cannot be distinguished, and are almost completely eroded. The crater in this velocity regime begins to take on a "vase" shape.

The initial diameter of the crater is essentially the diameter of the projectile at the crater entrance and increases with the depth of the crater. It is believed that the increase in crater diameter with crater depth is produced by both projectile expansion and spall. This phenomena was also observed in the wax targets of this study.

Between the velocities of 1.0 and 1.24 Km/sec, penetration effectiveness increases slowly as the projectile continues to erode.

Penetration data were also obtained using a flat-nosed projectile, and as expected, the penetration was much less than the solid projectile. The projectile and did not deform, and suffered only from slight surface erosion similar to that of the solid projectiles. Only one velocity was tested (6 shots); however, it is my belief that the penetration curve for this projectile configuration would approximately follow the dashed line of Figure 14. This conclusion is based on observations that projectile penetration curves produced by impacts at velocities less than that required to cause projectile deformation are generally linear with respect to velocity for a given projectile shape. The flat-nosed configuration is a higher drag configuration as indicated by the ballistic data from References [14], [15], and [16].

Penetration tests were also conducted with unmodified high velocity projectiles (off-the-shelf projectiles with the thin copper-alloy jacket intact). The unmodified projectiles produced deeper craters than the modified projectiles. This phenomenon can be explained by the increased resistance to deformation (strength) added by the copper-alloy jacket. These data are also plotted on Figure 14, and provide another example of the effect projectile-strength has on the penetration effectiveness.

Impacts into Wax Targets

Penetration data obtained during this study for lead projectiles impacting wax targets (13 cm. diam., and 30 cm. thick) are presented in Figure 16. Similar penetration characteristics are evident in both the wax-target and the Celotex-target data. At low velocities ($V_p < 0.3$ Km/sec), the penetration depth increases rapidly with increasing impact velocity. At an impact velocity of approximately 0.35 Km/sec, projectile penetration begins to decrease with increasing impact velocities. Again, the decrease in penetration effectiveness is marked by projectile mass loss (see Figure 17). At impact velocities above approximately 0.6 Km/sec, the penetration efficiency begins to increase again with impact velocity at a more gradual rate than at the lower impact velocities (Figure 16). These observations are expected for impacts involving relatively strong projectiles and weak targets.

As was observed in the data obtained from impacts into Celotex and lead targets, projectile shape is a variable in the effectiveness of projectile penetration at the lower velocities. At an impact velocity of approximately 1.2 Km/sec, the penetration curves for the solid and hollow point projectile converge. Solid-projectile deformation was not evident at impact velocities below 0.3 Km/sec, and the penetration curve is a strong function of impact velocity for impacts in the low-velocity impact regime. Projectile deformation occurred at impact velocities above 0.3 Km/sec for both the hollow-point and solid projectiles; however, the hollow-point projectiles deformed more extensively and more consistently than did the solid projectiles, and produced wider and shallower craters. Between the impact velocities of 0.3 and 0.4 Km/sec, the solid projectiles produced craters of varying depths, depending on the amount of deformation the projectile substained during the early stage of impact (see Figure 18). Impacts in the velocity regime between 0.3 and 0.4 Km/sec appear to produce pressures large enough to produce plastic deformation in the lead projectiles. It is believed that small variations in the strength and density of the wax targets produced various amounts of deformation. Because all impact tests conducted using wax targets were done at the same ambient temperature, the variation in target strength and density are believed to stem from the various pouring methods used in making the wax targets. Some targets were poured in layers allowing each layer to cool before pouring the next layer, and other targets were produced by filling the target mold in one pouring. Targets produced in one pouring shrank and developed cracks and voids during solidification.

At impact velocities above approximately 0.7 Km/sec, the crater depth increases steadily as the projectiles continue to erode with increasing impact velocities. Projectile fragments in the crater cavity also expanded the crater direction in the radial dimension in this velocity regime. At an impact velocity of approximately 1.2 Km/sec, the projectile is 50% eroded and the crater has expanded nearly to the hemispherical shape characteristic of the hypervelocity impact regime. This phenomenon may be explained by the earlier observation that the impact velocity required to initiate the hypervelocity impact phenomena for wax projectiles impacting wax targets is below 1.0 Km/sec, and an impact velocity of approximately 1.2 Km/sec was required to produce the hypervelocity phenomena when impacting lead projectiles into lead targets. It is not sufficient to state that the "hypervelocity regime" for a particular impact event has been reached based solely on the impact velocities required to produce the hypervelocity phenomena for impacts between targets and projectiles constructed from the same material. It should be noted, that the hypervelocity impact regime has not been reached, for a particular impact scenario, until the impact velocity is sufficient to produce pressures that greatly exceed the material strengths of both the projectile and target materials.

Impacts into Aluminum Targets

Lead projectiles were fired into aluminum targets (15 cm. diam., 10 cm thick) in this study to characterize impacts of relatively weak projectiles in strong targets. Impact velocities were between 0.20 and 1.24 Km/sec. These are relatively low impact velocities as compared to the impact velocity required to produce the hypervelocity impact phenomena in aluminum (Vp = 5.0 to 6.0 Km/sec); however, the impact velocity range tested is adequate to demonstrate the low-velocity impact phenomena.

As can be seen in Figure 19, the penetration curve is characteristic of impacts that occur between relatively weak projectiles and relatively strong targets at the lower velocities (see Figure 3).

Impact velocities below approximately 0.2 Km/sec produced essentially no penetration into the target, and the projectile merely deformed on the target surface.

At impact velocities between 0.3 and approximately 0.7 Km/sec, projectile penetration produced craters that were much larger in radius than in depth. There were essentially no measurable differences in volumes or depths of the craters produced from impacts of hollow point, solid, or flat-nosed projectiles. The hollow point projectiles did produce the characteristic "tit" at the bottom of the impact craters similar to that created in the lead targets.

Penetration depths continued to increase with impact velocities above 0.7 Km/sec; however, the impact craters produced began to vary drastically in shape from craters produced at the lower impact velocities. Impact craters began to resemble the vase-shape (narrow at the entrance, enlarging radially with depth). The characteristic crater "tit" produced by hollow point projectiles was no longer present. The "vase" shape crater increased in size as the impact velocity was increased; however, the hemispherical crater characteristic of the hypervelocity impact regime were not obtained at an impact velocity of 1.24 Km/sec. For materials such as aluminum, hypervelocity impact phenomena are not produced at impact velocities below 6 Km/sec.

Implications about Long-Rod Penetration

The development and shape characteristics of craters observed in this study imply some of the characteristics of craters produced by impacts of long-rod penetrators. Although the L/D of the projectiles used for this program were relatively small (L/D ≃ 3), some aspects of the craters obtained were observed to be similar to craters produced by much longer rod projectiles. As mentioned before, it is believed by many in the impact community that the penetration depth of the long-rod penetrator is limited for a given projectile material and length. The penetration curve for the long-rod penetrator of given length rises rapidly with velocity in the low-velocity regime and is believed by many in the technical community to approach asymptotically some maximum value. Figure 20 presents a plot of crater depth normalized to the rod length as a function of impact velocity for high strength steel rods impacting thick steel armor. As with Figure 20, Figure 7 is also used to verify the existence of the maximum penetration depth of a long-rod penetrator. The two examples of long-rod penetration effectiveness (Figures 7 and 20) do not include data at impact velocities considered to trigger the hypervelocity response of the projectile/target materials used in the tests. The characteristic crater produced by impacts of long-rod penetrators are long and narrow, and not at all similar to the hemispherical crater characteristic of chunky-projectile impacts in the hypervelocity regime. The long-rod penetration crater is characteristic of the penetration craters produced by the relatively short projectiles (L/D = 3) of this study at impact velocities below that required to initiate the radial expansion of the craters in lead, Celotex, and wax targets. It is suggested therefore that at much higher impact velocities the impact crater of the long-rod penatrator will begin to expand radially, approaching the hemispheric shape characteristic of chunky (L/D = 1) projectiles and will continue to expand as the impact velocity is increased. I believe that the region of little or no increase in penetration may be marked by relatively large increases in crater volume as the impact crater expands to the hemispherical shape. The range of impact velocities at which there is no strong increase in penetration effectiveness is expected to be a function of the penetrator L/D and of the material properties of the projectile and target. Once the hemispherical crater shape is obtained, the penetration efficiency is expected to again increase, approximately, as the 2/3 power of the impact velocity. Figure 21 represents the penetration trends expected to be produced by long-rod penetrators.

CHAPTER VI

EMPIRICAL ANALYSIS

Most empirical equations predict penetration depths fairly well above the impact velocities at which a hemispherical crater is produced, and are specified to be valid only over that impact velocity range (see Figure 22). Empirical equations used to model impacts at velocities below the threshold required to produce hemispherical craters use mechanical properties of the target and/or projectile materials to predict the penetration depth. As indicated by others [4, 17, 18] and by the data produced in this study, another factor that influences the penetration effectiveness of a projectile is the design strength and/or shape of the projectile.

The empirical equation developed in this study allows for variations in projectile design in the first term, and is the form

$$P/L = a\left(\frac{\rho_p}{\rho_t}\right)^{1/2} / V_p^2 \exp^{(|b - V_p|^d / V_p)} + k\left(\frac{\rho_p}{\rho_t}\right)^{1/2} V_p^{2/3} . \tag{41}$$

The first term of Equation (41) represents the steady-state penetration phase of the impact, and the second term represents the cavitation phase of the penetration. There are several terms in Equation (41) that are common to many of the other correlations presented in this study. The first term contains the fluid-jet expression and an expression that varies the penetration depth with impact velocity and projectile design. The second term contains part of the fluid-jet equation and the impact velocity raised to the 2/3 power. The constants (a, b, d, k) are obtained experimentally. The constants, a and k, are used to match the predictions to the data and appear to be influenced by the material strengths of the target/projectile combination. The constant, b, tends to vary as a function of the impact velocity required to deform the target subtracted from the impact velocity required to deform the projectile. The constant, d, is the term used to define the projectile geometric effects on penetration. Comparisons of test data from this study and predictions obtained from Equation (41) are presented in Figures 23 - 25. Comparisons are also presented in Figures 23, and 26 - 33 for data obtained from other impact studies. The data from the impact tests used in the comparisons are presented in Tables 3 - 11.

It is demonstrated in Figures 23 - 33, that Equation (41) can be made to fit the penetration data over a wide range of projectile/target materials and designs; however, as with all empirical equations, not all penetration data can be fit using this equation, and it should only be used as a rule-of-thumb. Another observation pertains to material-strength effects on crater formation. As described previously, the hypervelocity impact regime has been defined as impacts occurring at velocities above the speed of sound in the materials of the colliding objects. The pressures generated under these conditions exceed the material strengths by factors of 10 - 1000, and material response is believed to be governed solely by an equation of state. In this regime, solids are treated as fluids and the expressions used to predict the penetration effectiveness of a projectile are based primarily on the density ratio of the projectile and target (hydrodynamic codes) [19]. It is widely expected in the impact community that the hypervelocity-impact regime for most structural metals is reached at impact velocities between 5 - 6 Km/sec. The data presented in Figure 28 indicate that the penetration effectiveness of an aluminum projectile impacting aluminum targets is influenced by the target strength at impact velocities up to approximately, and perhaps beyond, 7 Km/sec.

CHAPTER VII

CONCLUSIONS AND RECOMMENDATIONS

Impact phenomena are not clearly understood, thus the prediction of observed crater dimensions is a difficult task. Several predictive techniques are available that aid in the prediction of the impact process; however, designers of systems required to withstand impacts or penetrate targets must conduct impact experiments for accurate assessment of the systems designed. A better understanding of the impact process, and the factors influencing the process at all impact velocities, is required. Normal impacts of chunky ($L/D \simeq 3$) lead projectiles into finite targets were conducted to verify current impact theory and evaluate several factors that influence the penetration process.

From knowledge that exists about the impact process, a limited amount of information can be ascertained about impact events such as fragments from explosions, and meteor strikes on spacecraft. With known material properties of both the projectile and target, crude estimates of impact velocity and projectile shape can be made, based on the residual crater dimensions and shape. Experiments are currently being conducted at various agencies in an attempt to develop a passive means to capture intact projectiles, traveling at hypervelocity speeds, by allowing the projectile to penetrate into underdense targets. A media is considered underdense when the bulk density is much less than that of the material used create the media (e.g., expanded foams) [20].

The penetration depth of an intact high-velocity projectile into an underdense target will vary with the properties of the projectile and target materials, the impact velocity, and the shape of the projectile.

This study also verifies the projectile design influences on the characteristic penetration curve and crater shape. The effects of projectile design on the impact crater are evident up to impact velocities at which the variations in initial projectile geometry are rendered negligible early in the penetration process. Projectiles that differ in design over a significant body length require much higher impact velocities before the penetration curves merge than do projectiles that differ in design for only a small percentage of the body length. In essence, the penetration efficiency varies for projectiles of different designs during the steady-state penetration phase, until the differences in the projectiles have been eroded. The penetration curves tend to merge for projectiles of different designs once the contributions to crater depth due to projectile differences are negligible as compared to the overall crater depth.

I also suggest that the crater depth produced by a long-rod penetrator does not reach a maximum value, but will continue to increase as a function of increasing impact velocity after some region of little or no increase in penetration depth. During the impact-velocity region of little or no increase in crater depth, it is expected that the impact crater will expand in the radial direction, marked by a significant increase in crater volume, and approach a hemispherical crater. Once the hemispherical crater is obtained, the penetration efficiency is expected to increase with increasing impact velocity. It is suggested that additional long-rod impact tests be conducted using projectiles and targets constructed of relatively soft materials (i.e., lead) and with rods of L/D approximately 6 to 8; these parameters reduce the impact velocities required to characterize the penetration mechanics beyond the steady-state penetration regime.

Target material strength has also been shown to have an effect on the crater depth produced from impacts at and above impact velocities considered to be in the hypervelocity impact regime. The supporting data for this conclusion were obtained from impacts of projectile and target materials of equal density. Heat treatment of the target material was used to vary the material strength. It is recommended that further impact testing be done using other target and projectile materials of similar density and varying strengths in order to better understand the role that material strength plays in the penetration process.

LIST OF REFERENCES

LIST OF REFERENCES

1. Zukas, J. A., et al. Impact Dynamics. New York: John Wiley and Sons, Inc., 1982.

2. Charters, A. C. "High Speed Impact." Scientific American. Vol. 203, No. 4, October 1960, pp. 128-140.

3. Herrmann, W., and Wilbeck, J. "Review of Hypervelocity Penetration Theories." Proceedings of the 1986 Hypervelocity Impact Symposium: International Journal of Impact Engineering. Vol. 5, Nos. 1-4, October 1986, pp. 307-322.

4. Zukas, J. A., Ed. High Velocity Impact Dynamics. New York: John Wiley and Sons, Inc., 1990.

5. Christman, D. R. and Gehring, J. W. "Analysis of High-Velocity Projectile Penetration Mechanics." Journal of Applied Physics. Vol. 37, No. 4, 15 March 1966, pp. 1579-1587.

6. Goodier, J. N. "On the Mechanics of Indentation and Cratering in Solid Targets of Strain - Hardening Metal by Impacts of Hard and Soft Spheres." Proceedings of the Seventh Hypervelocity Impact Symposium. Vol. 3, February 1965, pp. 215 - 259.

7. Gehring, J. W., Meyers, C. L., and Charest, J. A. "Experimental Studies of Impact Phenomena and Correlation with Theoritical Models." Proceedings of the Seventh Hypervelocity Impact Symposium. Vol. 5, February 1965, pp. 161-211.

8. Tate, A. "Long Rod Penetration Models - Part 1. A Flow Field Model for High Speed Long Rod Penetration." International Journal of Mechanical Science. Vol. 28, No. 8, 1986, pp. 535-548.

9. Tate, A. "Long Rod Penetration Models - Part 2. Extensions to the Hydrodynamic Theory of Penetration." International Journal of Mechanical Science. Vol. 28, No.9, 1986, pp. 599-612.

10. Miller, W. S., Ed. Machine Design: 1980 Materials Reference Issue. Vol. 52, No. 8, 17 April 1980, pp. 80 - 82.

11. Sorensen, N. R. "Systematic Investigation of Crater Formation in Metals." Proceedings of the Seventh Hypervelocity Impact Symposium. Vol. 6, February 1965, pp. 281-325.

12. Naumann, R. J. "A Physical Basis for Scaling Hypervelocity Impacts." Proceedings of the Seventh Hypervelocity Impact Symposium. Vol. 4, February 1965, pp. 1-33.

13. Walsh, J. M. and Johnson, W. E. "On the Theory of Hypervelocity Impact." Proceedings of the Seventh Hypervelocity Impact Symposium. Vol. 2, February 1965, pp. 1-75.

14. O'Brian, B., Ed. Guns and Ammo: 1991 Annual Buyers Guide. pp. 237-251.

15. Barnes, F. C. Cartridges of the World. 5th Ed. Northbrook, IL: DBI Books Inc., 1985.

16. Federal Cartridge Company. Ammunition Guide. Anoka NM., 1990.

17. Woodward, R. L. "The Effects of Projectile Tip Geometry on Penetration into Semi-infinite Metal Targets." Proceedings of the Ninth International Symposium on Ballistics. Shrivenham: Royal Military College of Science, 1986, pp. 431-437.

18. Wilkins, M. L. "Mechanics of Penetration and Perforation." International Journal of Engineering Science. Vol. 16, 1978, pp. 793-807.

19. Zukas, J. A., Segletes, S. B., and Furlong, J. R. "Numerical Simulation of Impact Phenomena." Scientific Computing and Automation. Vol. 7, No. 6, April 1991, pp. 15-29.

20. Tsou, P. "Intact Capture of Hypervelocity Projectiles." Proceedings of the 1989 Hypervelocity Impact Symposium: International Journal of Impact Engineering. Vol. 10, Nos. 1-4, December 1989, pp. 615 - 627.

SUPPLEMENTARY REFERENCES

Charters, A. C. and Menna, T. L. "Penetration Dynamics of Rods from Direct Ballistic Test of Advanced Armor Components at 2 - 3 Km/sec." Proceedings of the 1989 Hypervelocity Impact Symposium: International Journal of Impact Engineering. Vol. 10, Nos. 1-4, December 1989, pp. 93 - 106.

Christman, D. R., Wenzel, A. B., and Gehring, J. W. "Penetration Mechanisms of High - Velocity Rods." Proceedings of the Seventh Hypervelocity Impact Symposium. Vol. 6, February 1965, pp. 169-235.

Hohler, V. and Stilp, A. J. "Hypervelocity Inpacts of Rod Projectiles with L/D from 1 to 32." Proceedings of the 1989 Hypervelocity Impact Symposium: International Journal of Impact Engineering. Vol. 10, Nos. 1 - 4, December 1989, pp. 323-331.

Johnson, W. A., et al. "Mechanics of High Speed Impacts Between Rods and Plates." Journal of Mechanical Physics in Solids. Vol. 29, 1981, pp. 413-445.

Mobley, Jr., C. E., and Pond, R. B. "Energy Balance for Hypervelocity Targets." Proceedings of the Seventh Hypervelocity Impact Symposium. Vol. 6, February 1965, pp. 73-104.

Smithells, C. J., Ed. Metals Reference Book. 3rd Ed., Vol. 2, Washington: Butterworths and Company, 1962.

APPENDIXES

APPENDIX A

FIGURES

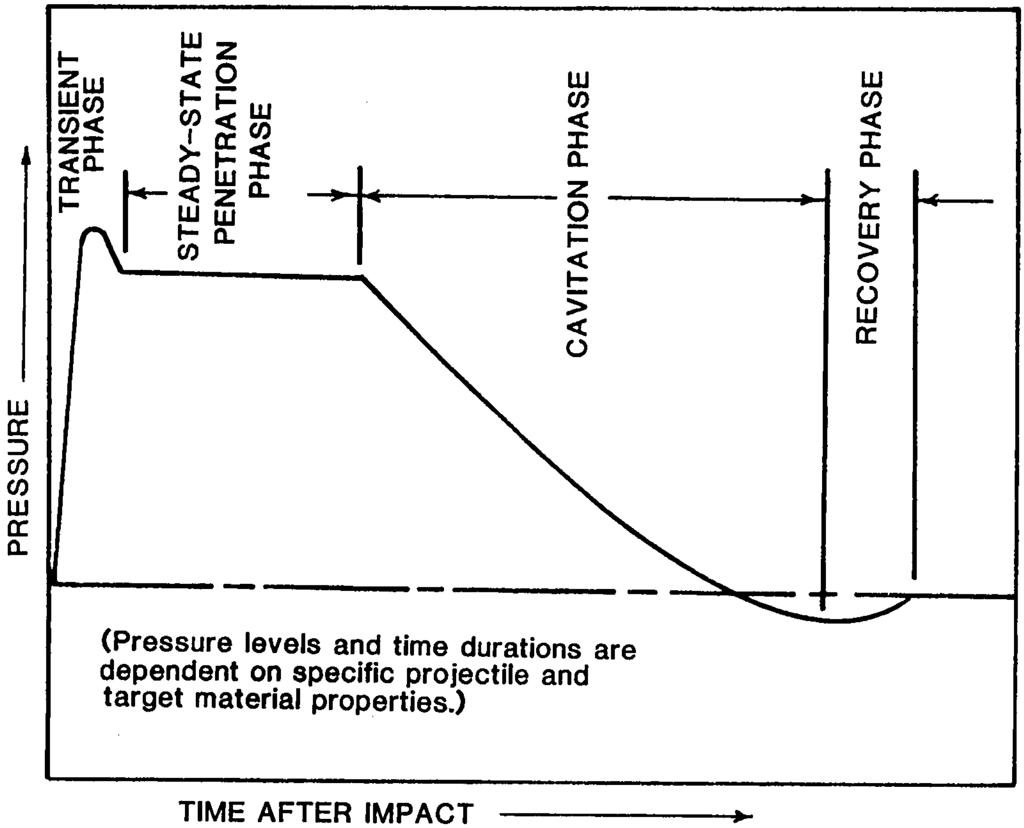

Figure 1. Impact Pressures During Impact [5]

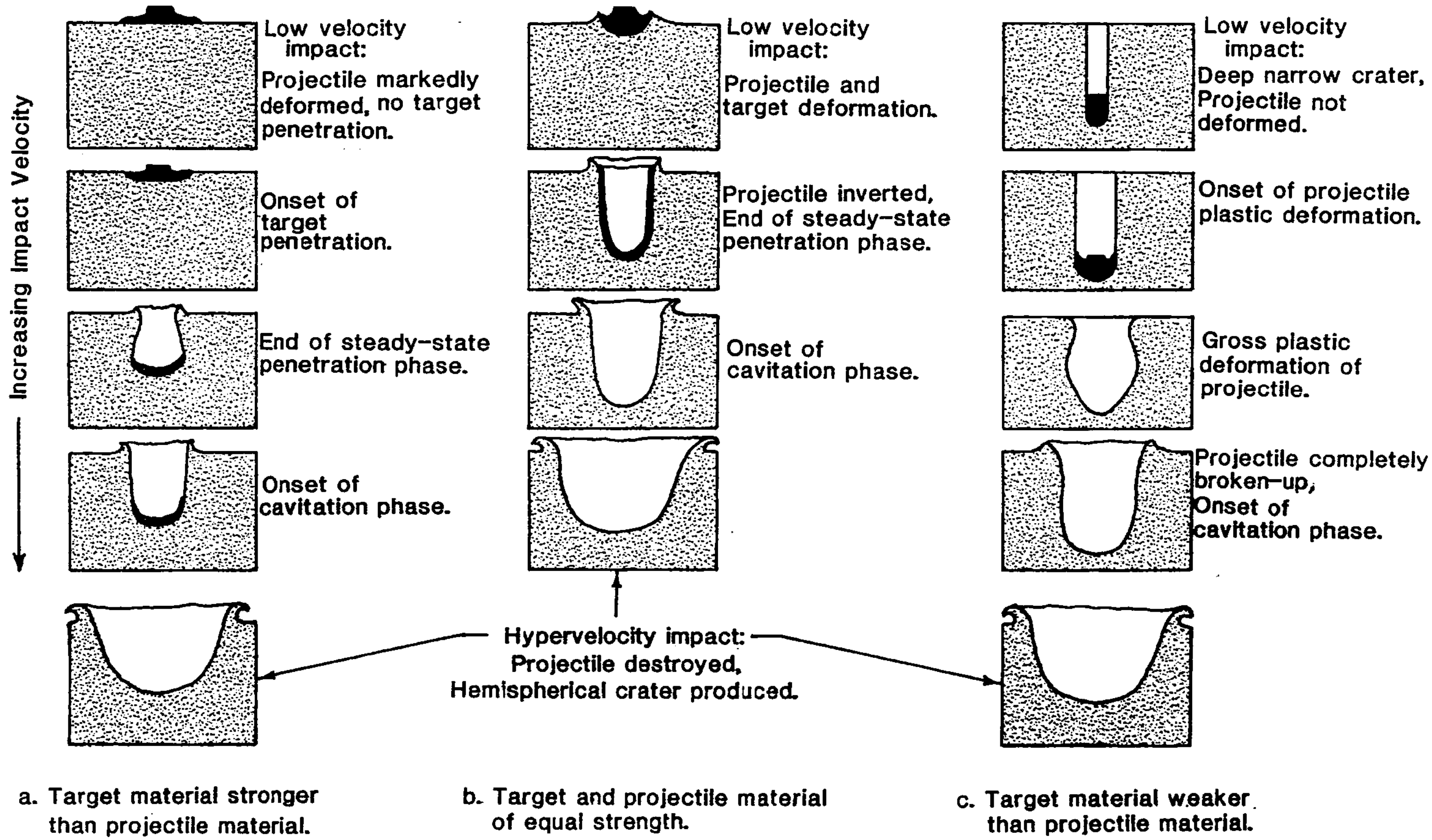

Figure 2. Schematic of Cratering Process

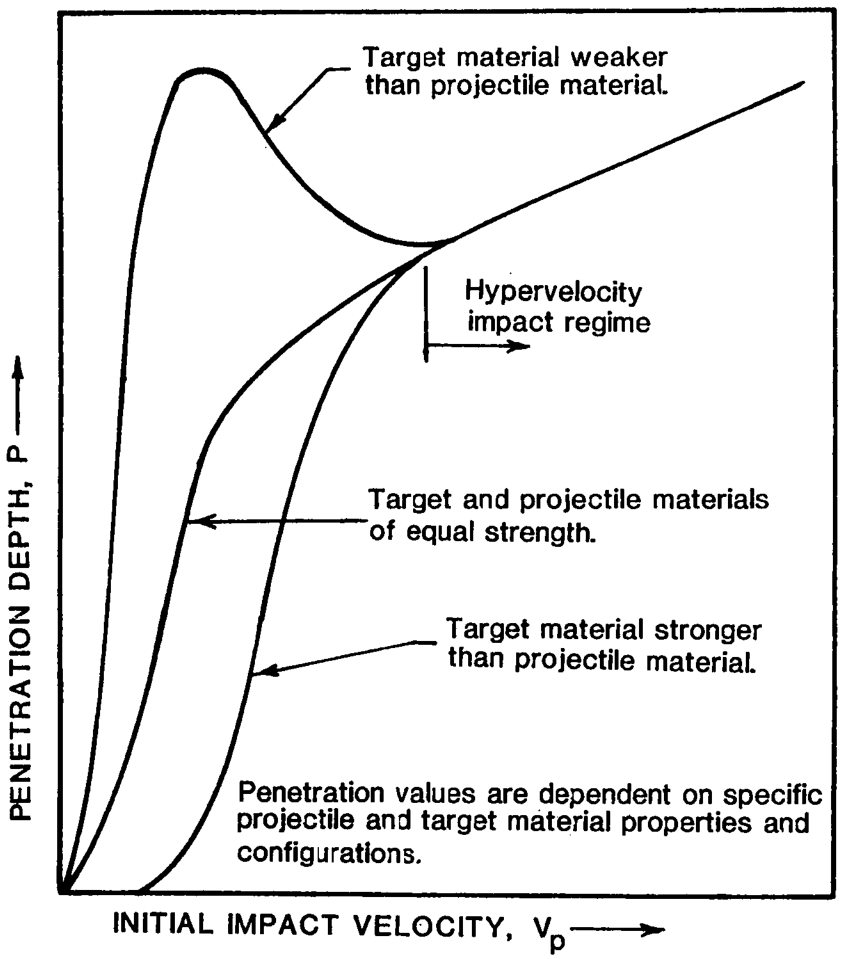

Figure 3. Characteristic Penetration Curves for Small L/D Projectiles Impacting Semi-infinite Targets

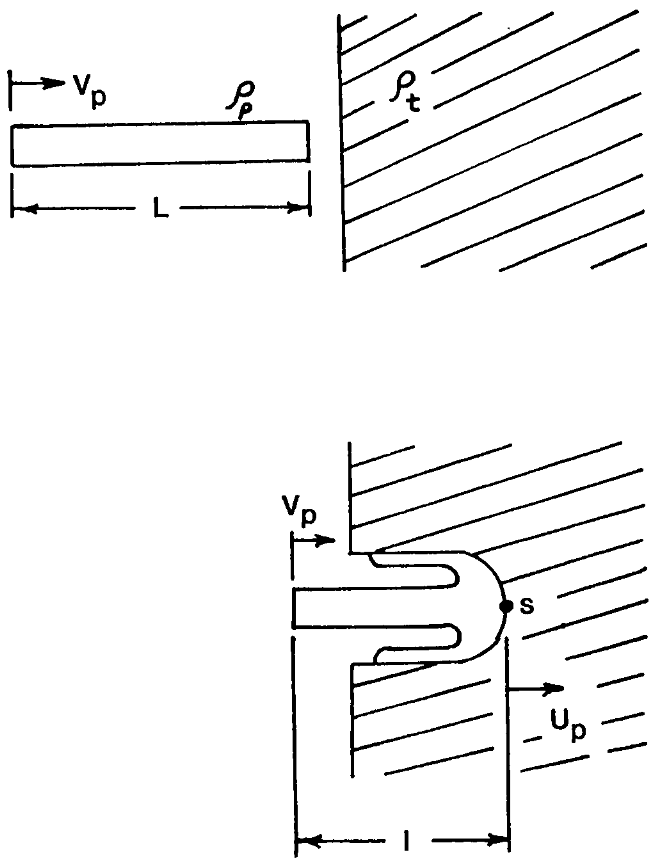

Figure 4. Material Flow in the Fluid Jet Model

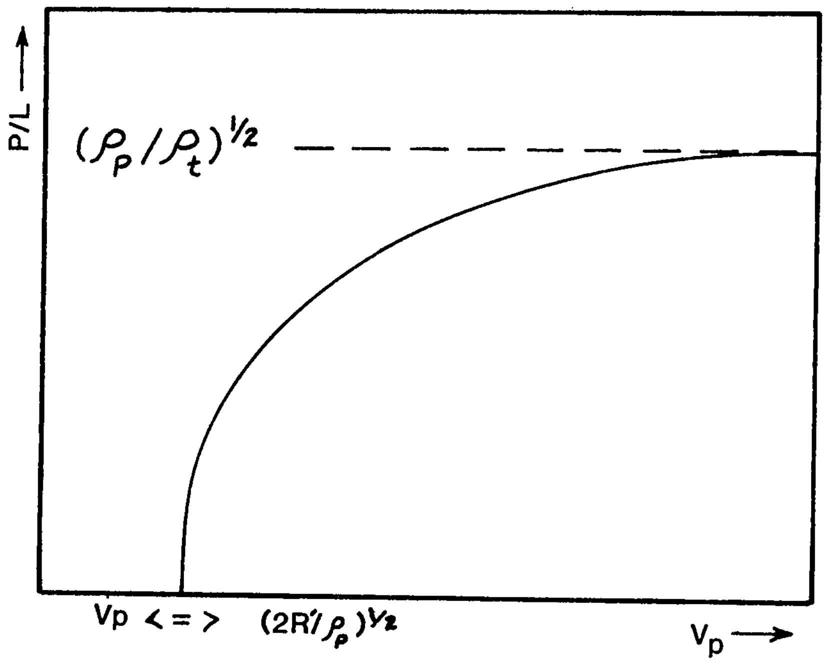

Figure 5. Schematic Penetration Curve Calculated by the Theory of Allen and Rodgers [4]

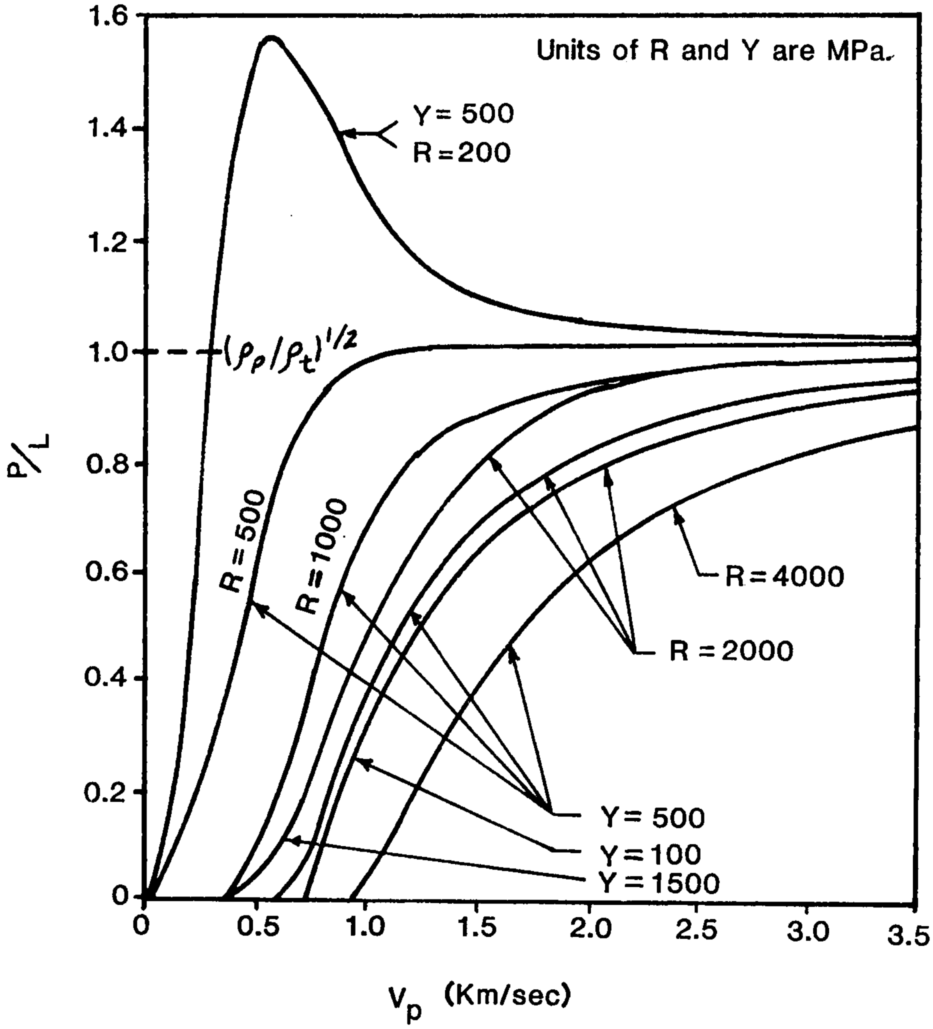

Figure 6. Tate and Alakseevskii Theoretical Penetration Curves for Steel Projectiles Impacting Steel Targets and Various Combinations of R and Y [4]

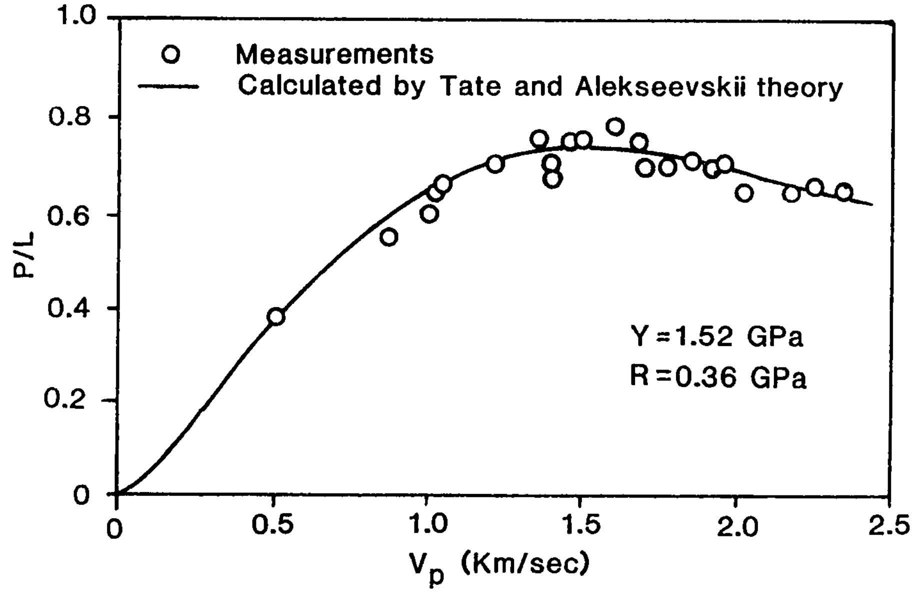

Figure 7. Penetration of Al-alloy Rods (L/D = 10) into Lead Targets [4]

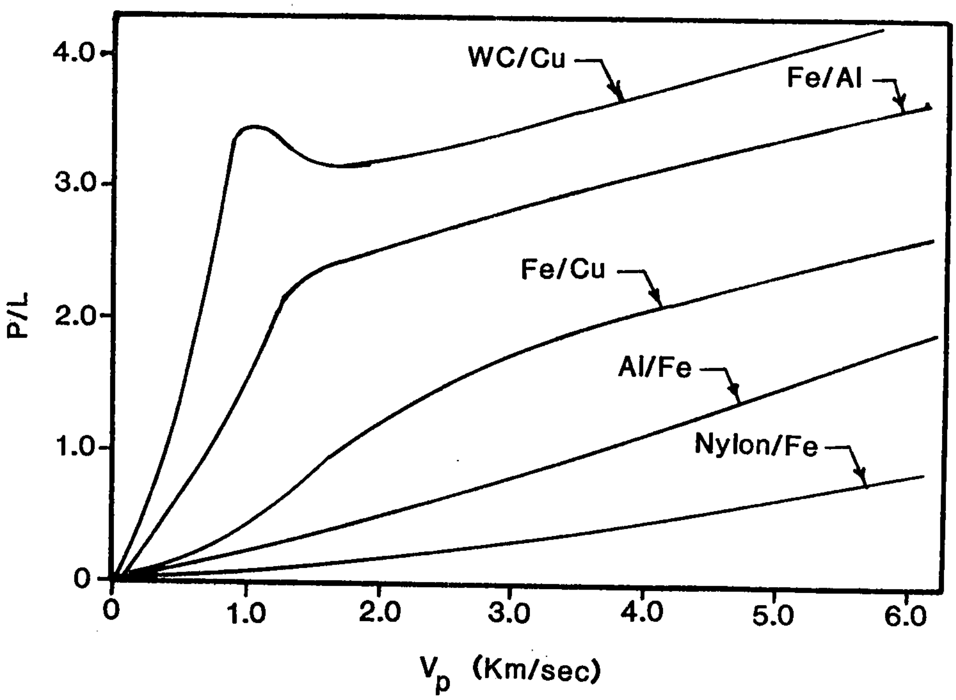

Figure 8. Impact Penetration Normalized to Projectile Length versus Impact Velocity for Several Projectile/Target Material Combinations as Predicted by Equation (34) [4]

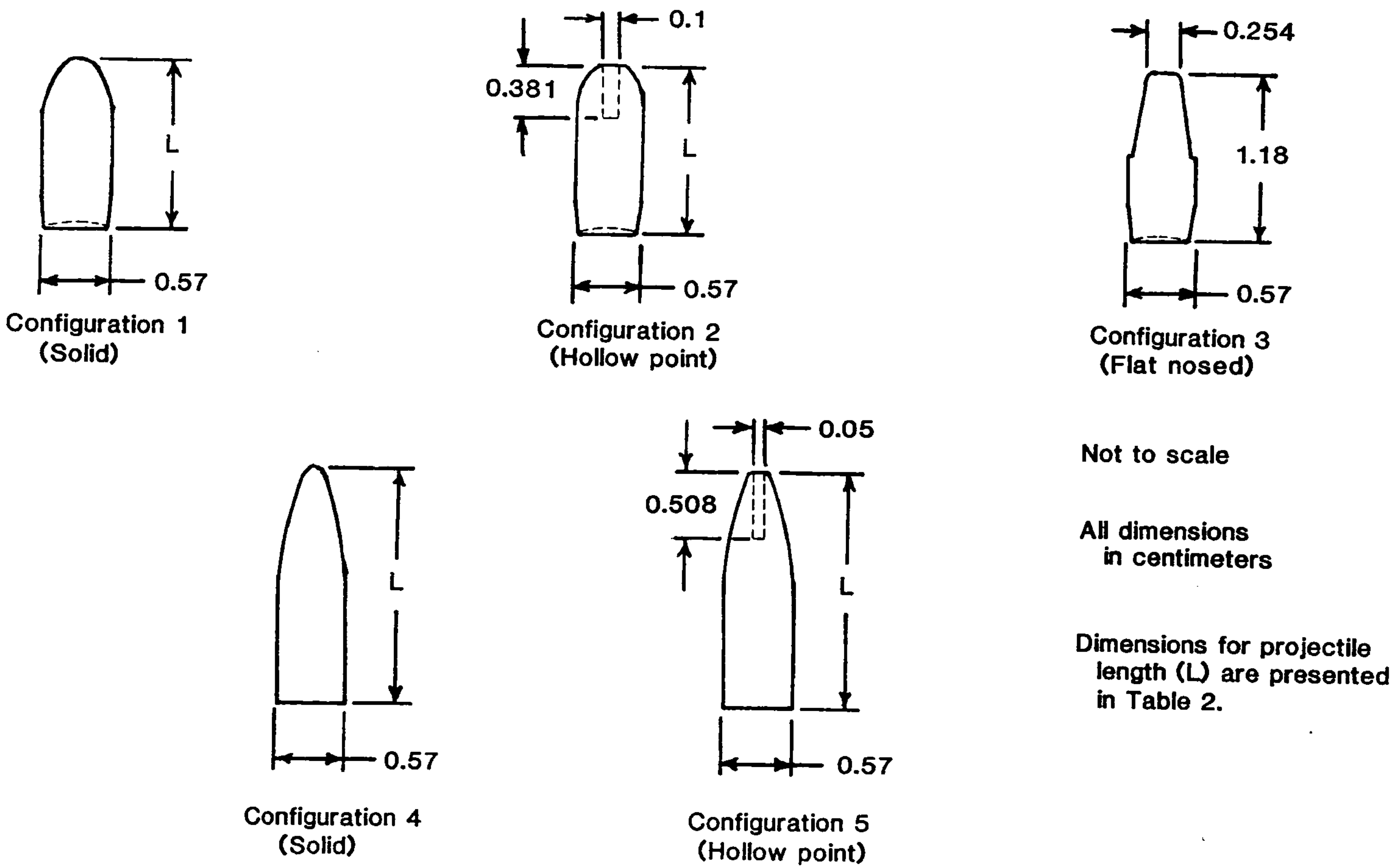

Figure 9. Projectile Configurations

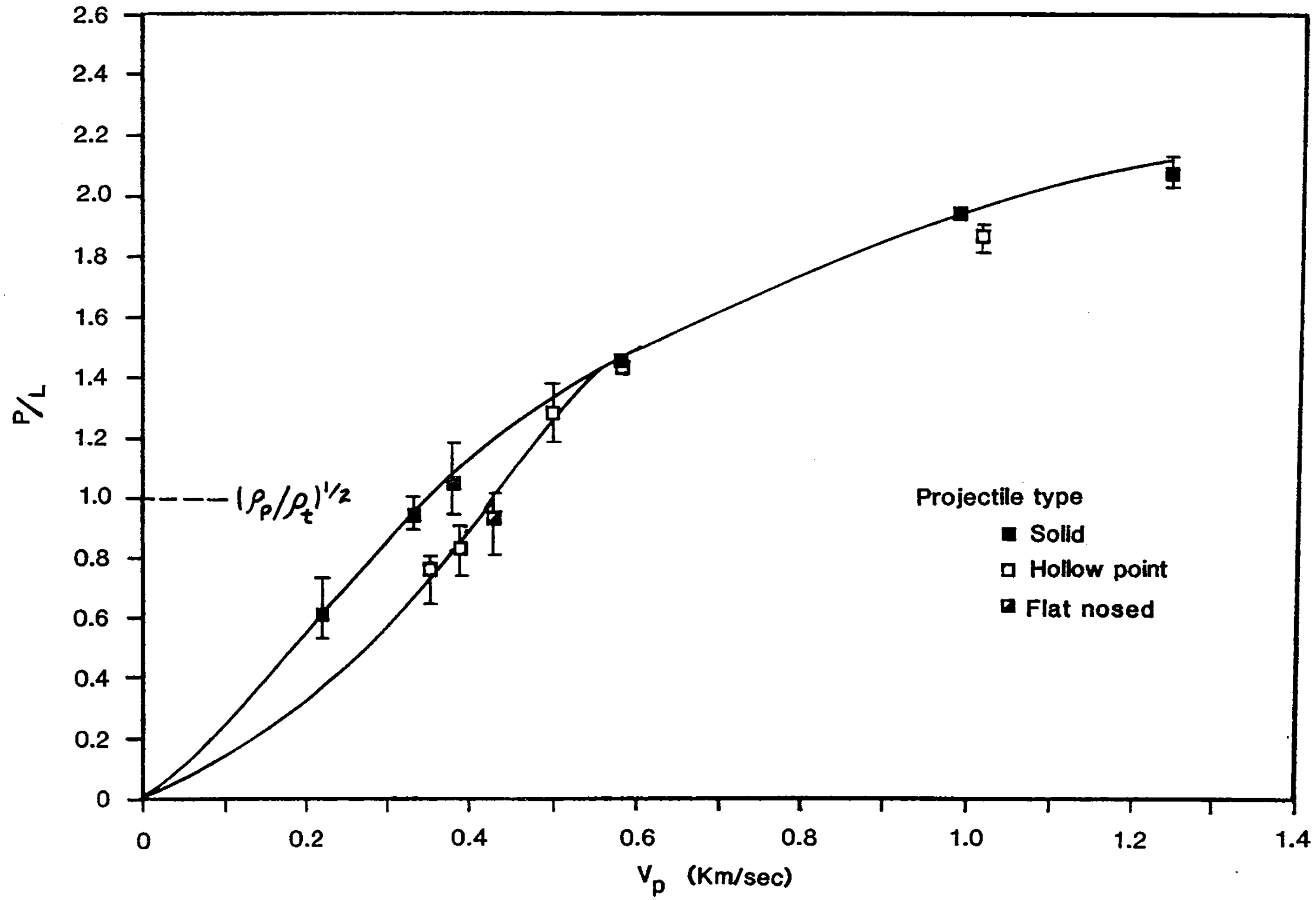

Figure 10. Penetration Effectiveness of Lead Projectiles into Lead Targets

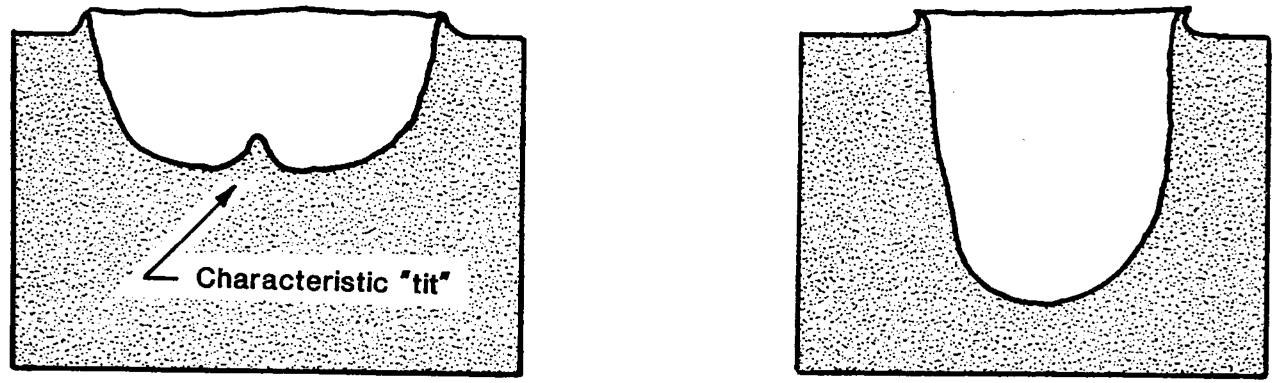

Characteristic crater produced by hollow–point projectiles (wide–shallow crater)

Characteristic crater produced by solid projectiles (narrow–deep crater)

Figure 11. Characteristic Craters Produced by Lead Projectiles Impacting Lead Targets at Impact Velocities Below 0.6 Km/sec

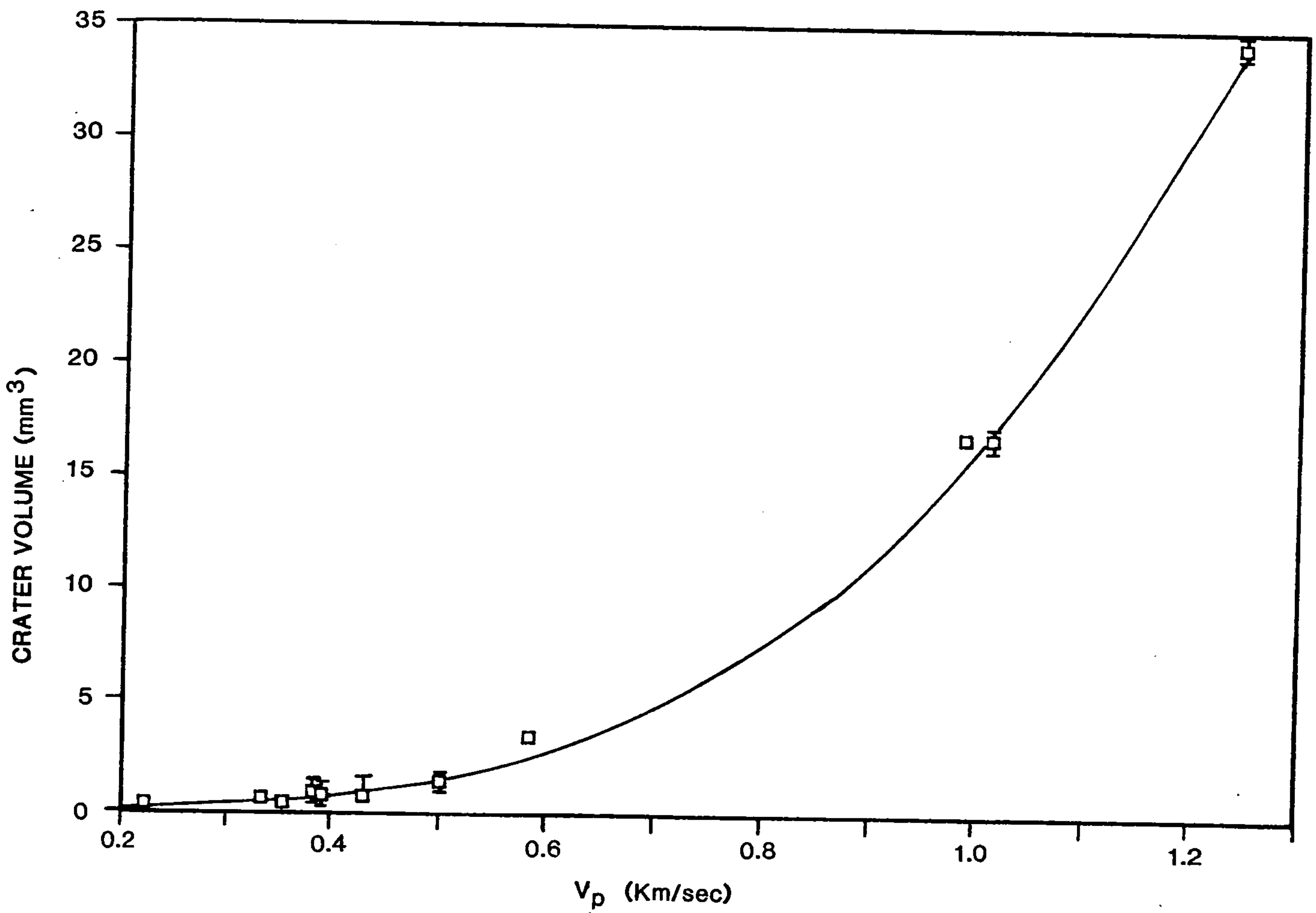

Figure 12. Crater Volumes Produced in Lead Targets

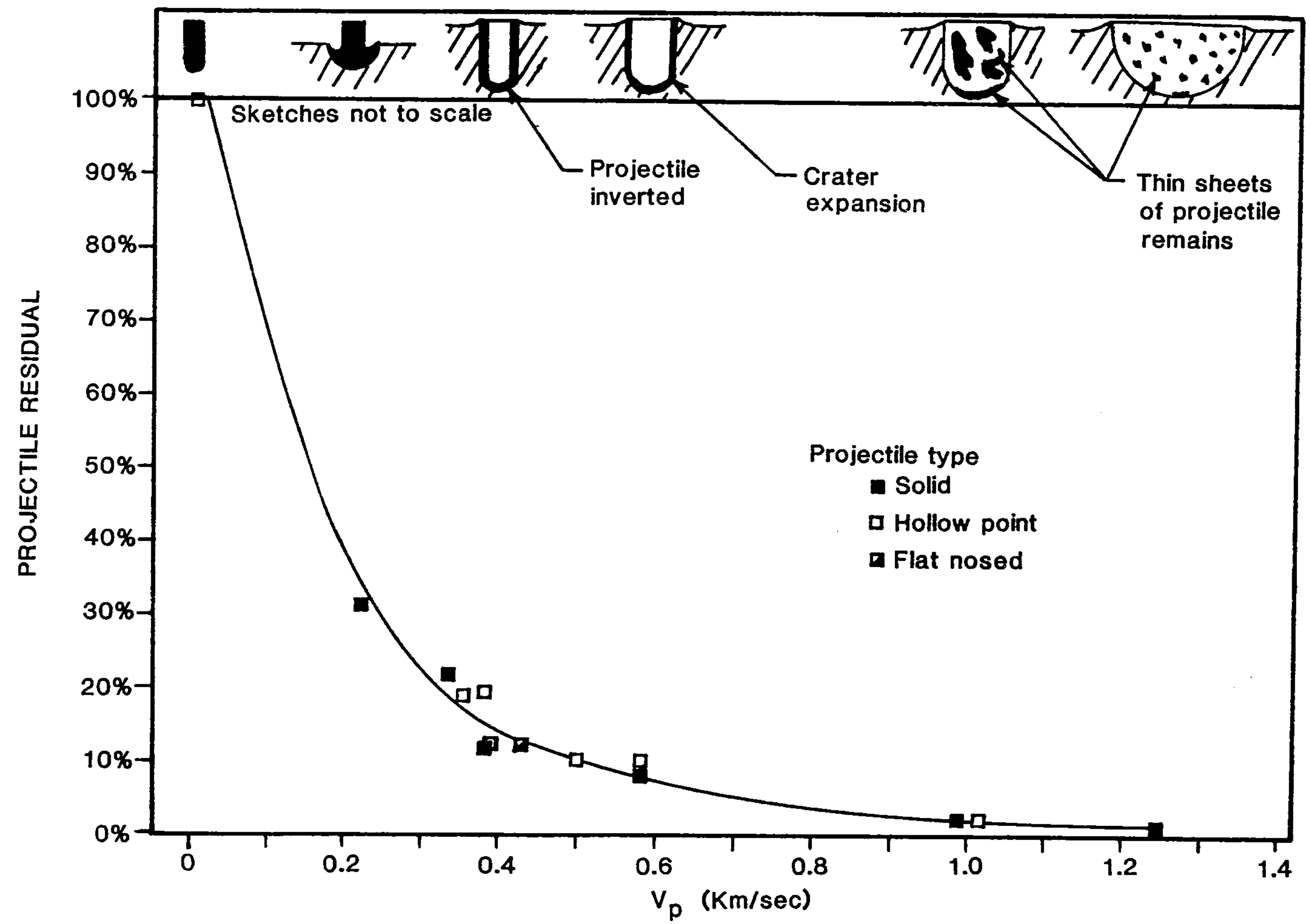

Figure 13. Lead Projectile Residual Thickness in Lead Craters Expressed in Percent of Pre-test Projectile Length

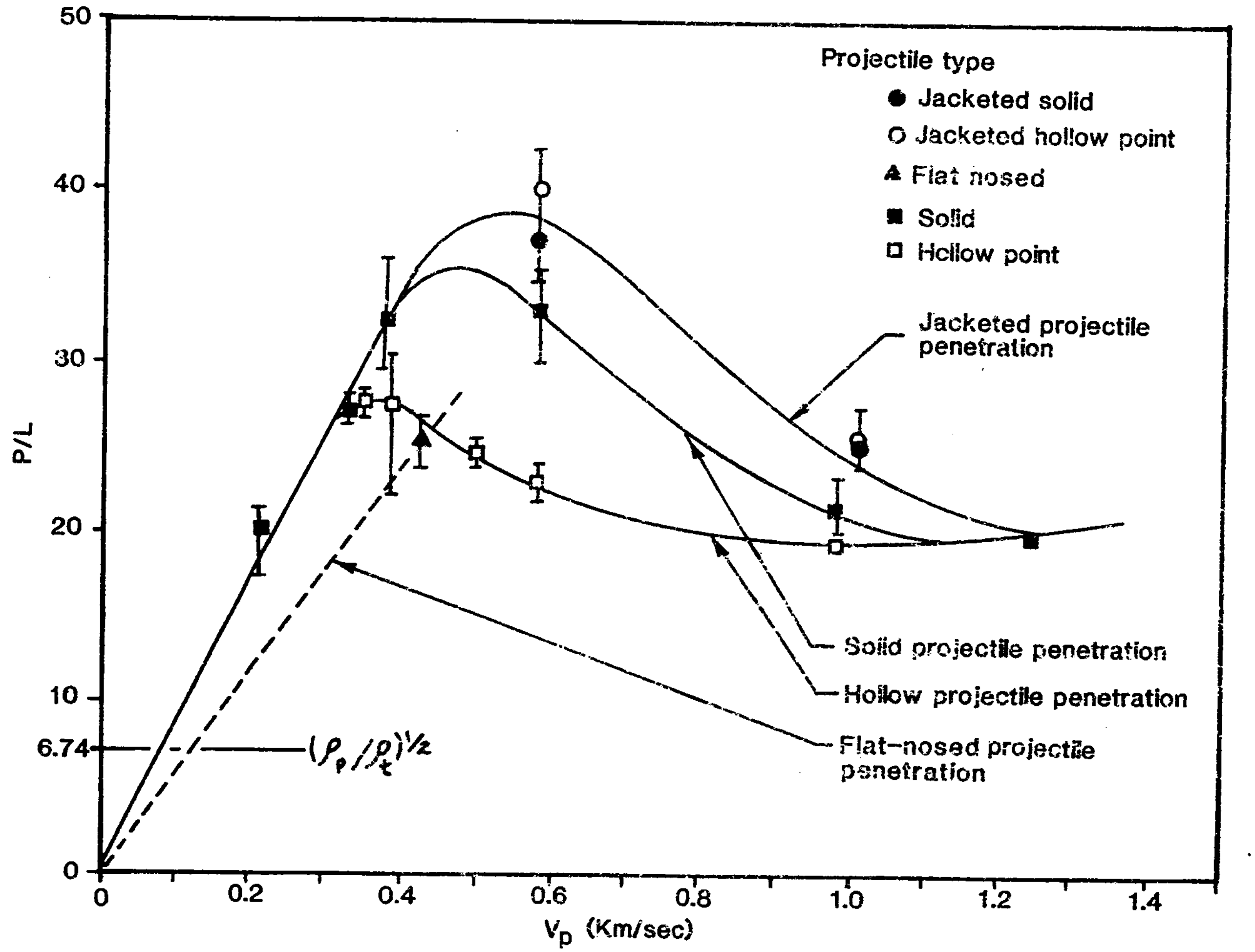

Figure 14. Penetration Effectiveness of Lead Projectiles into Celotex® Targets

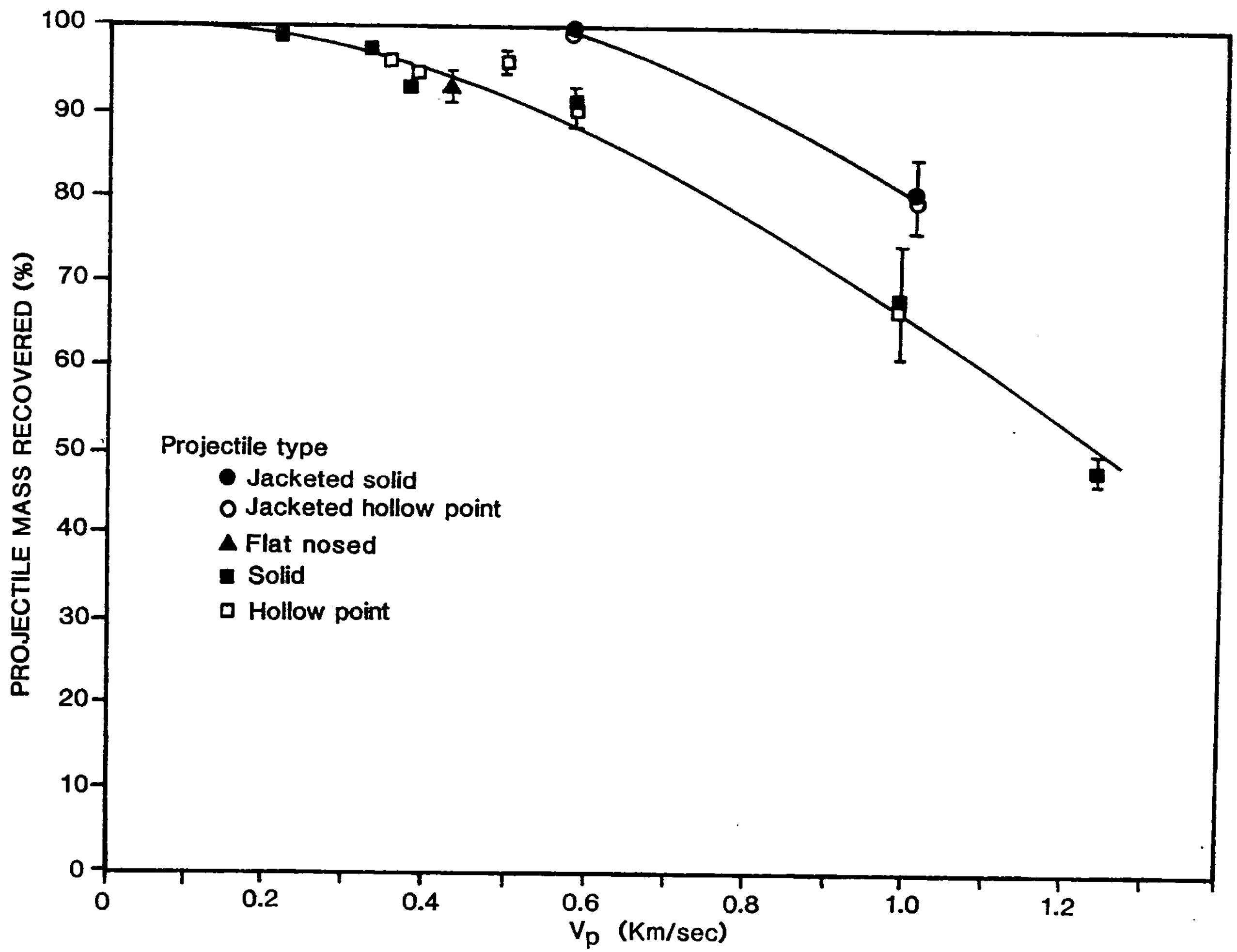

Figure 15. Projectile Mass Recovered from Impacts into Celotex® Targets

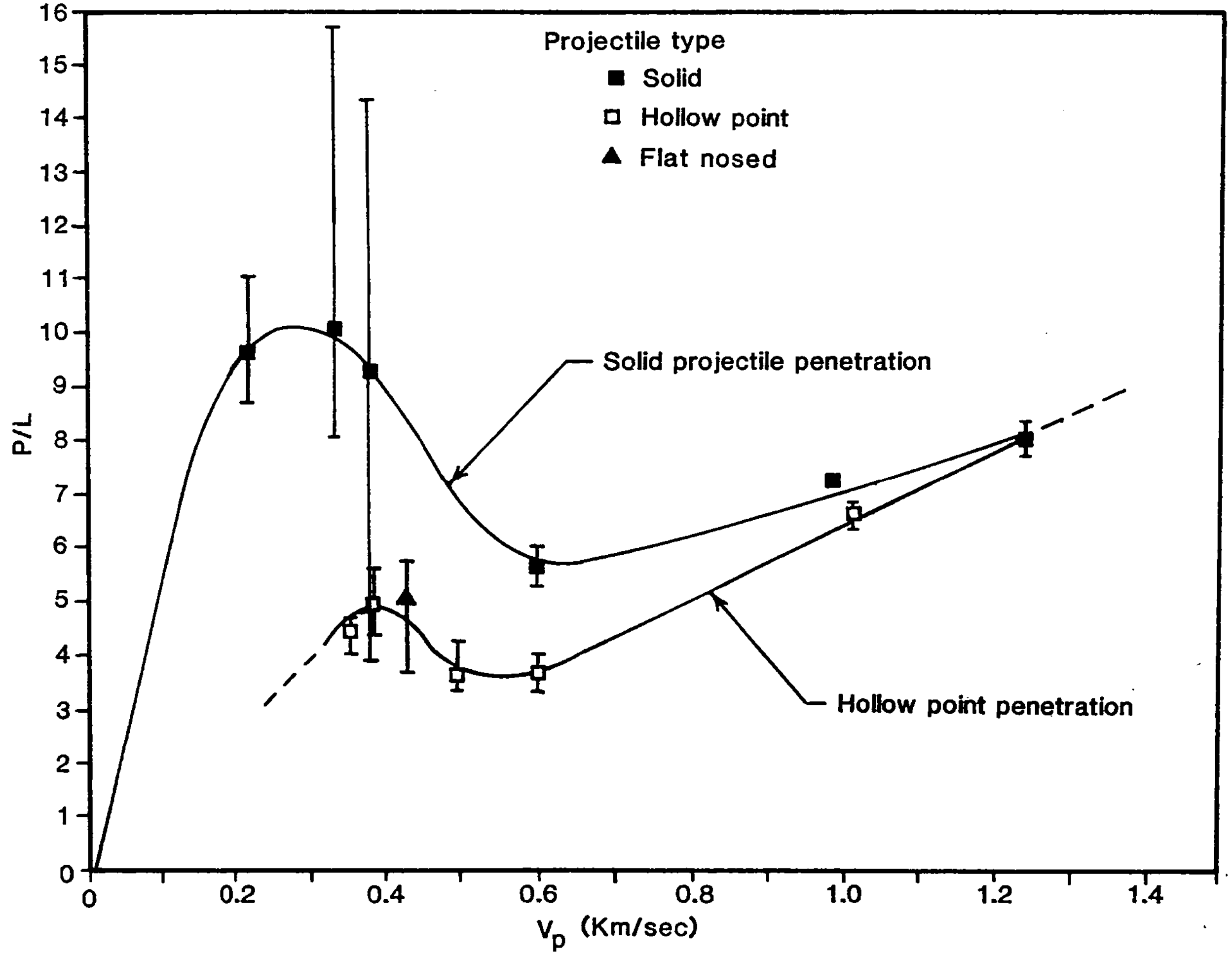

Figure 16. Penetration Effectiveness of Lead Projectiles into Wax Targets

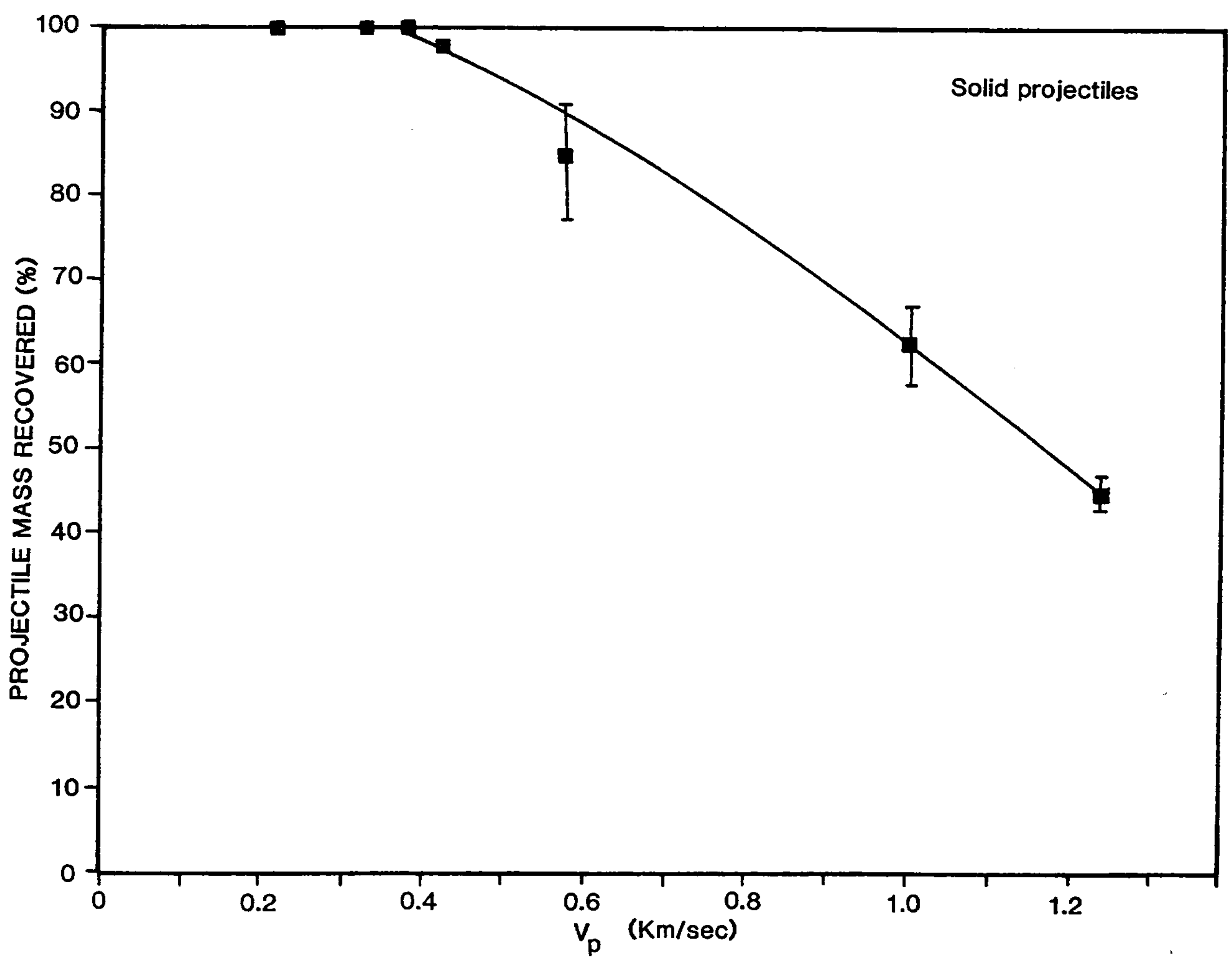

Figure 17. Projectile Mass Recovered from Impacts into Wax Targets

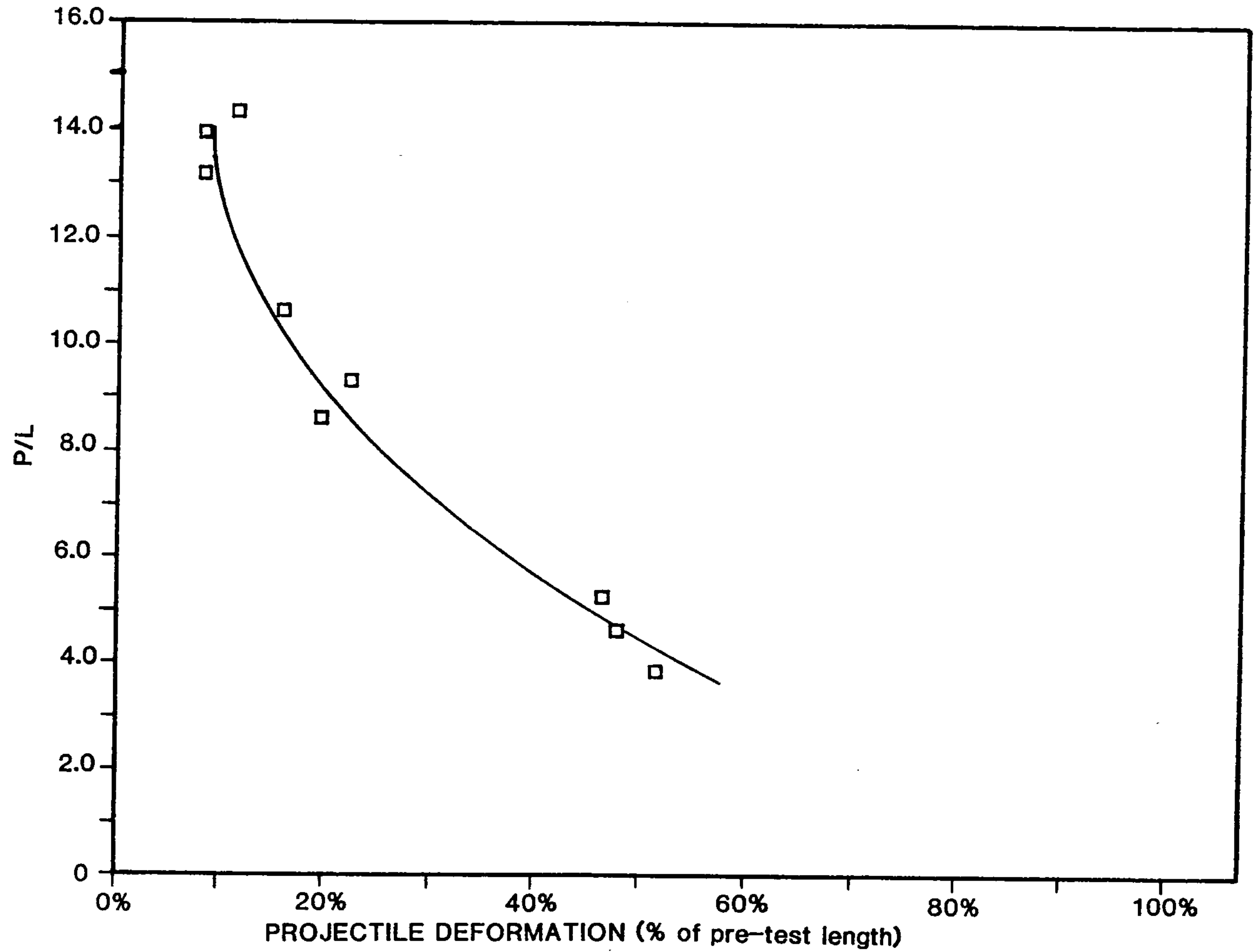

Figure 18. Penetration Effectiveness versus Projectile Deformation Expressed in Percent of Projectile Pre-test Length for Lead Projectiles Impacting Wax Targets at an Impact Velocity of 0.38 Km/sec

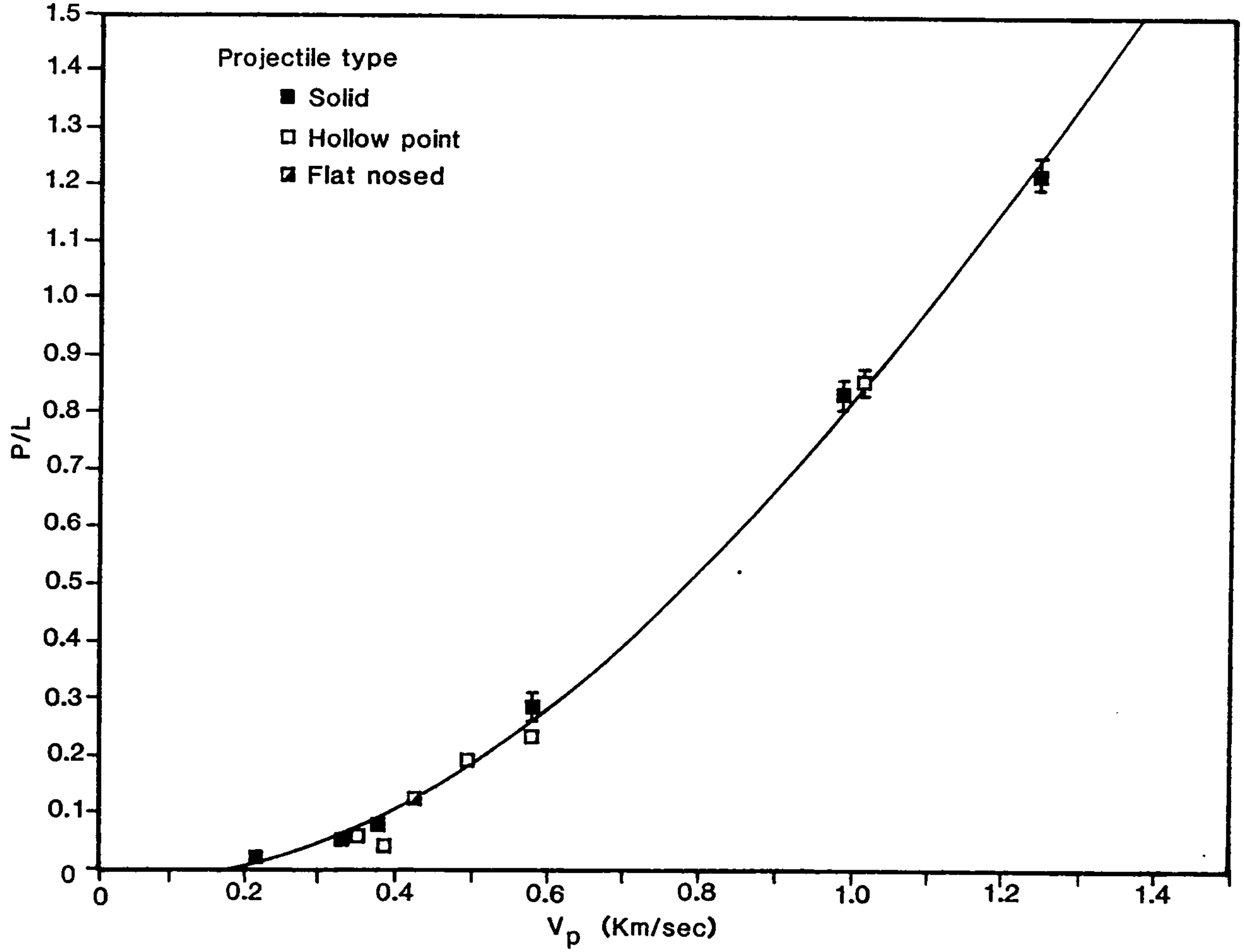

Figure 19. Penetration Effectiveness of Lead Projectiles into Aluminum (6061-T6) Targets

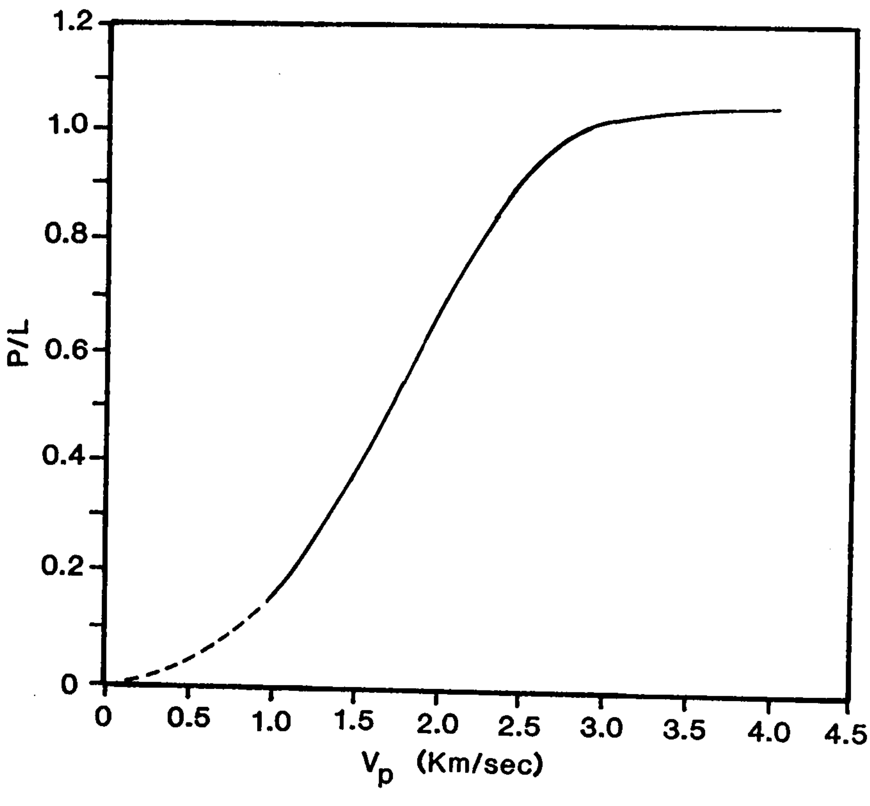

Figure 20. Normalized Rod-Penetration Depth versus Impact Velocity for Long-Steel Rods Impacting Thick-Steel Targets [1]

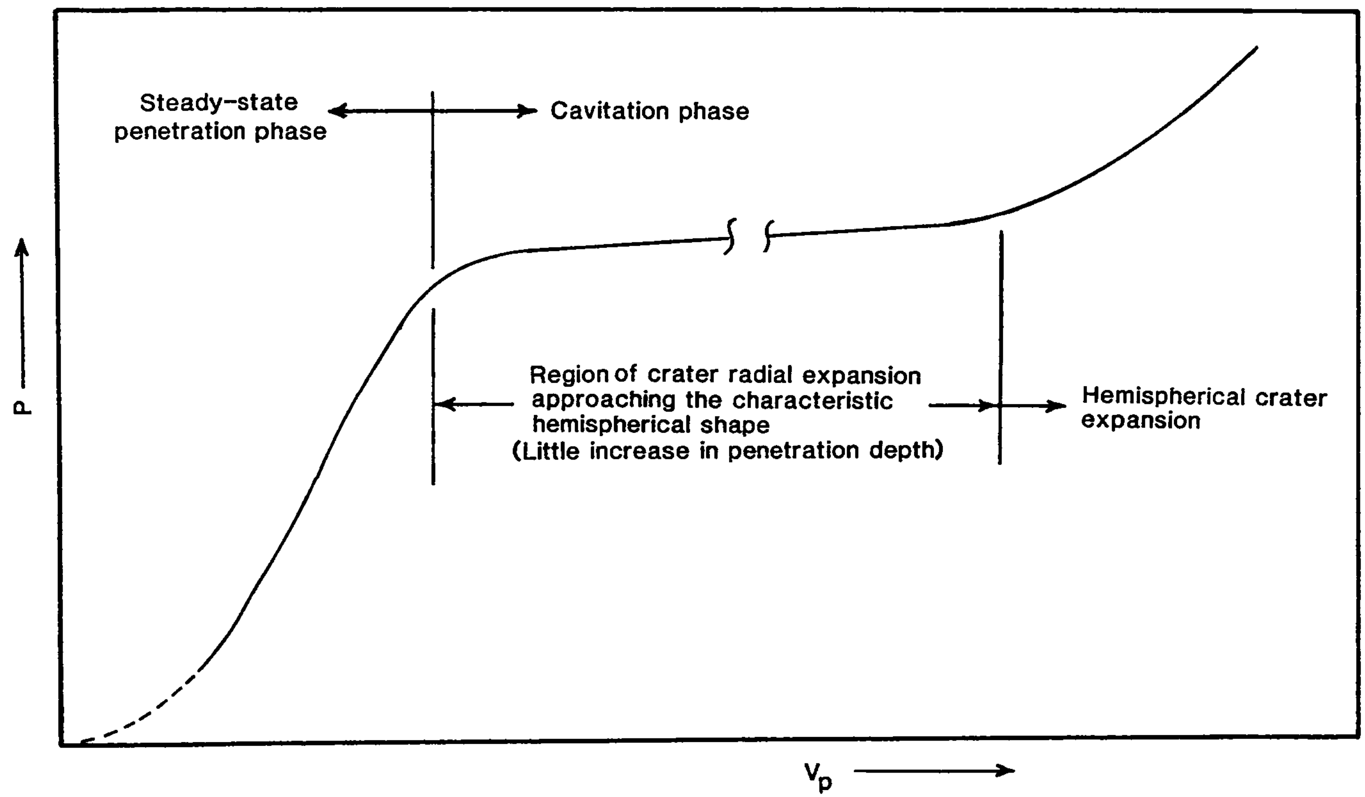

Figure 21. Expected Penetration Effectiveness of Long Rod Penetrators versus Impact Velocity

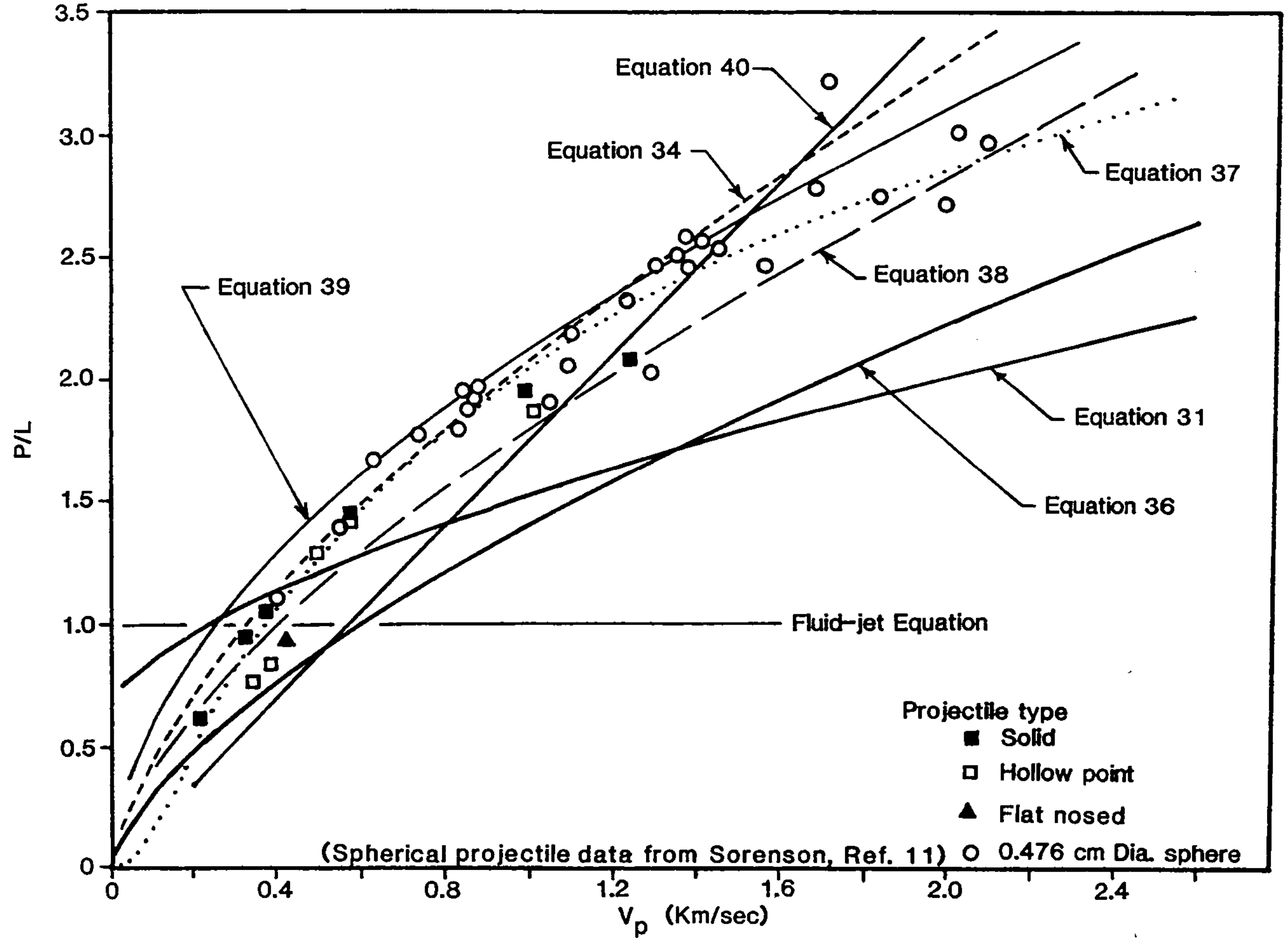

Figure 22. Comparisons of Theoretical Impact Models with Impact Data from Lead Projectiles Impacting Lead Targets

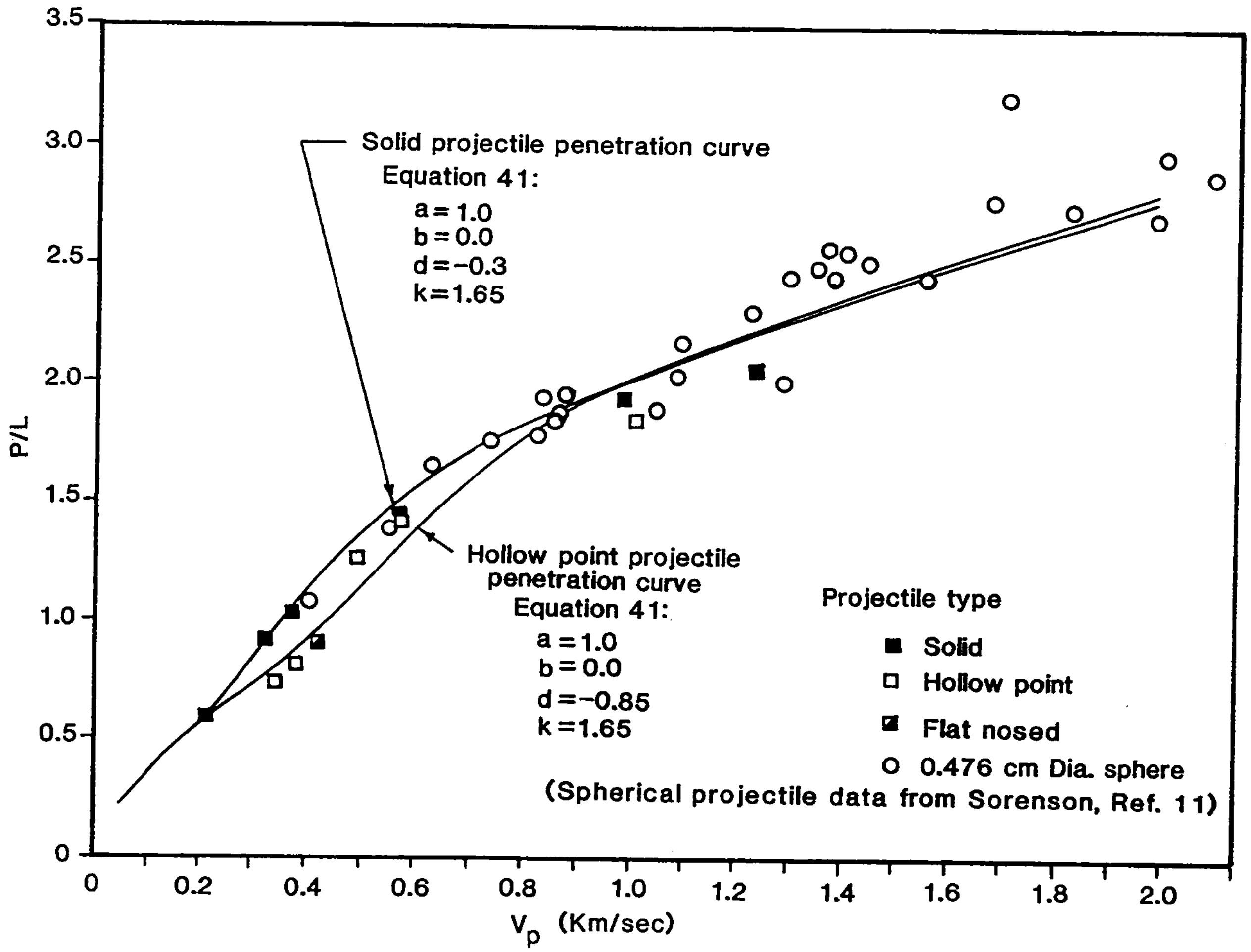

Figure 23. Penetration Curve of Lead Projectiles Impacting Lead Targets Calculated by Equation (41)

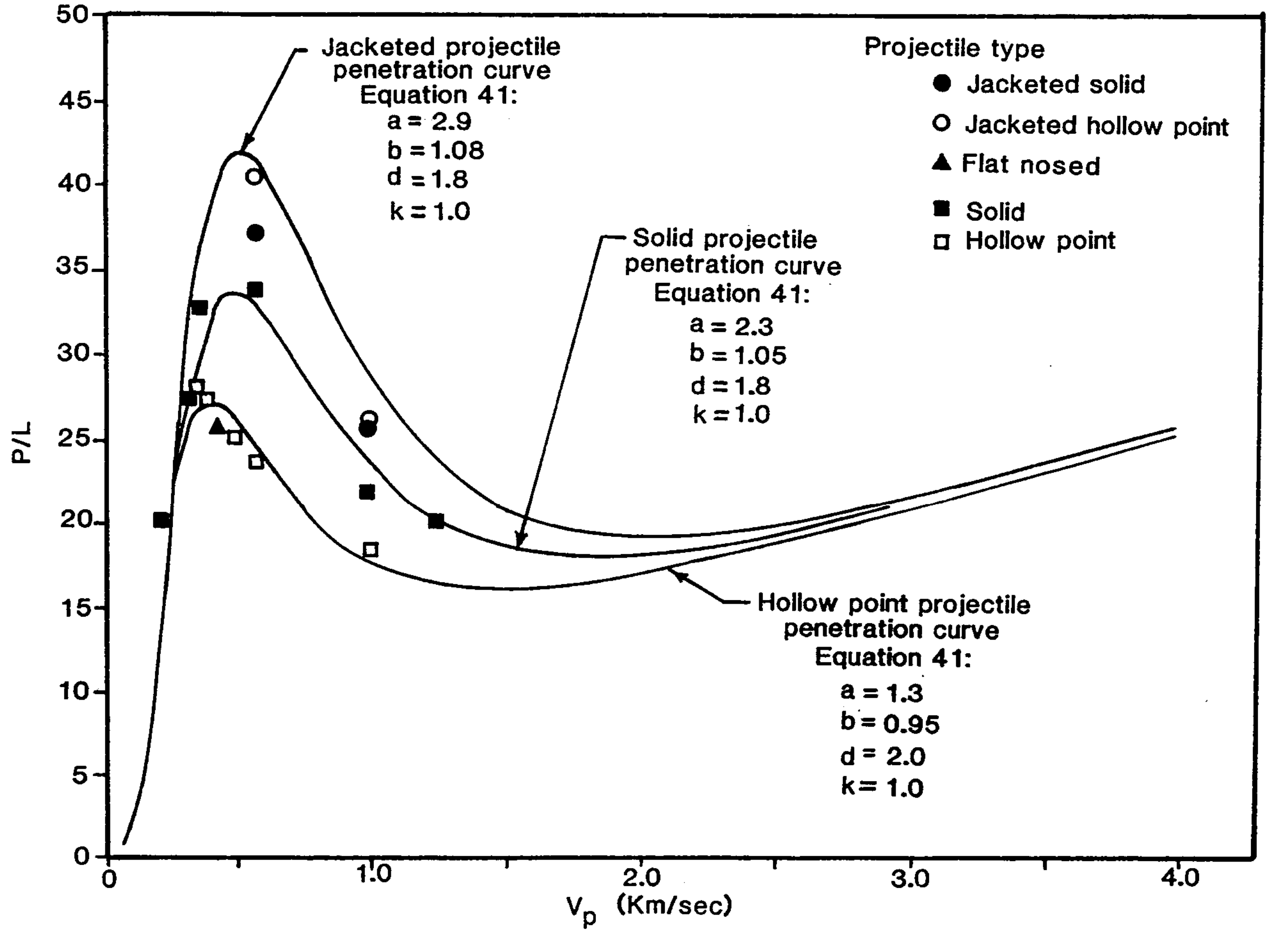

Figure 24. Penetration Curve of Lead Projectiles Impacting Celotex® Targets Calculated by Equation (41)

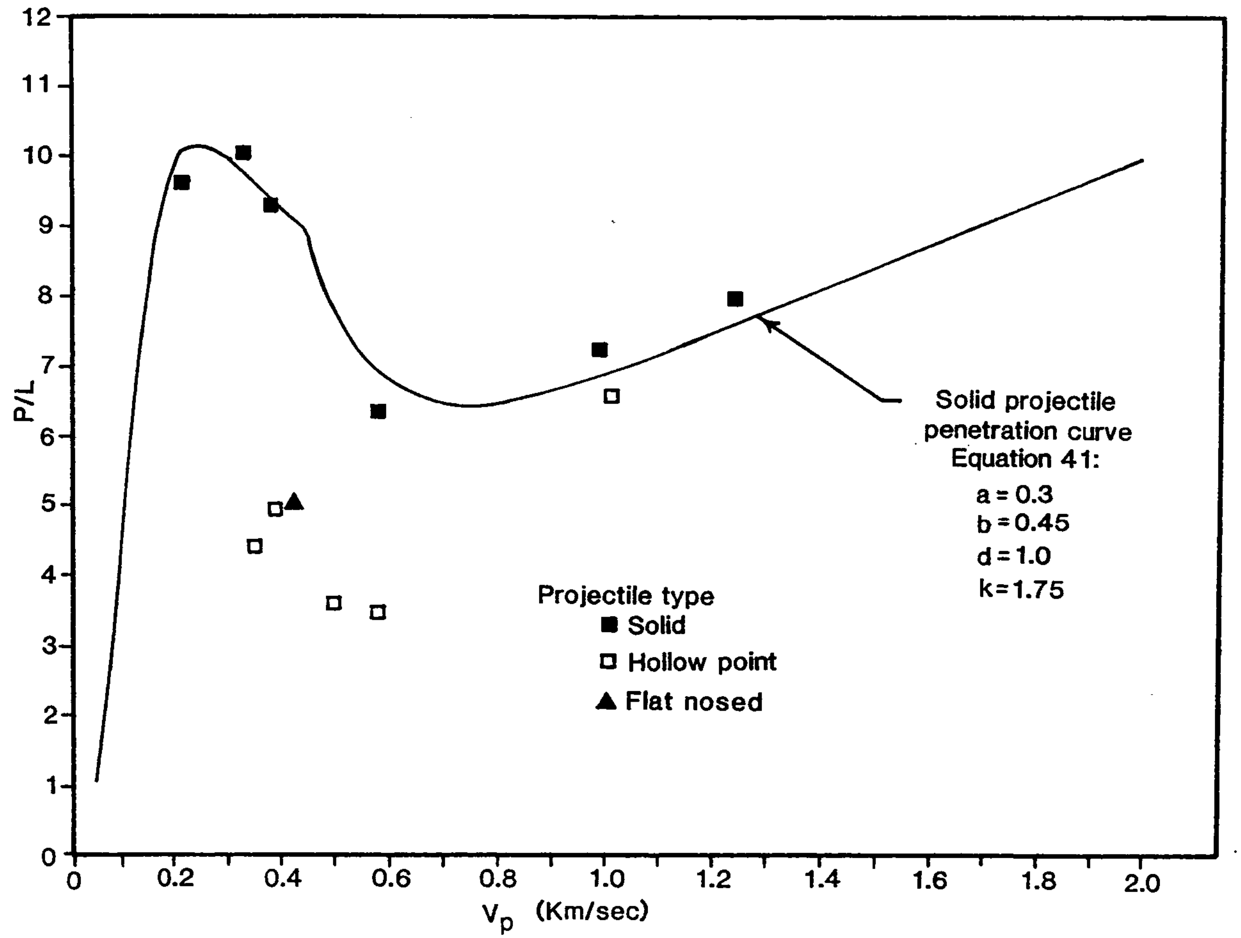

Figure 25. Penetration Curve of Lead Projectiles Impacting Wax Targets Calculated by Equation (41)

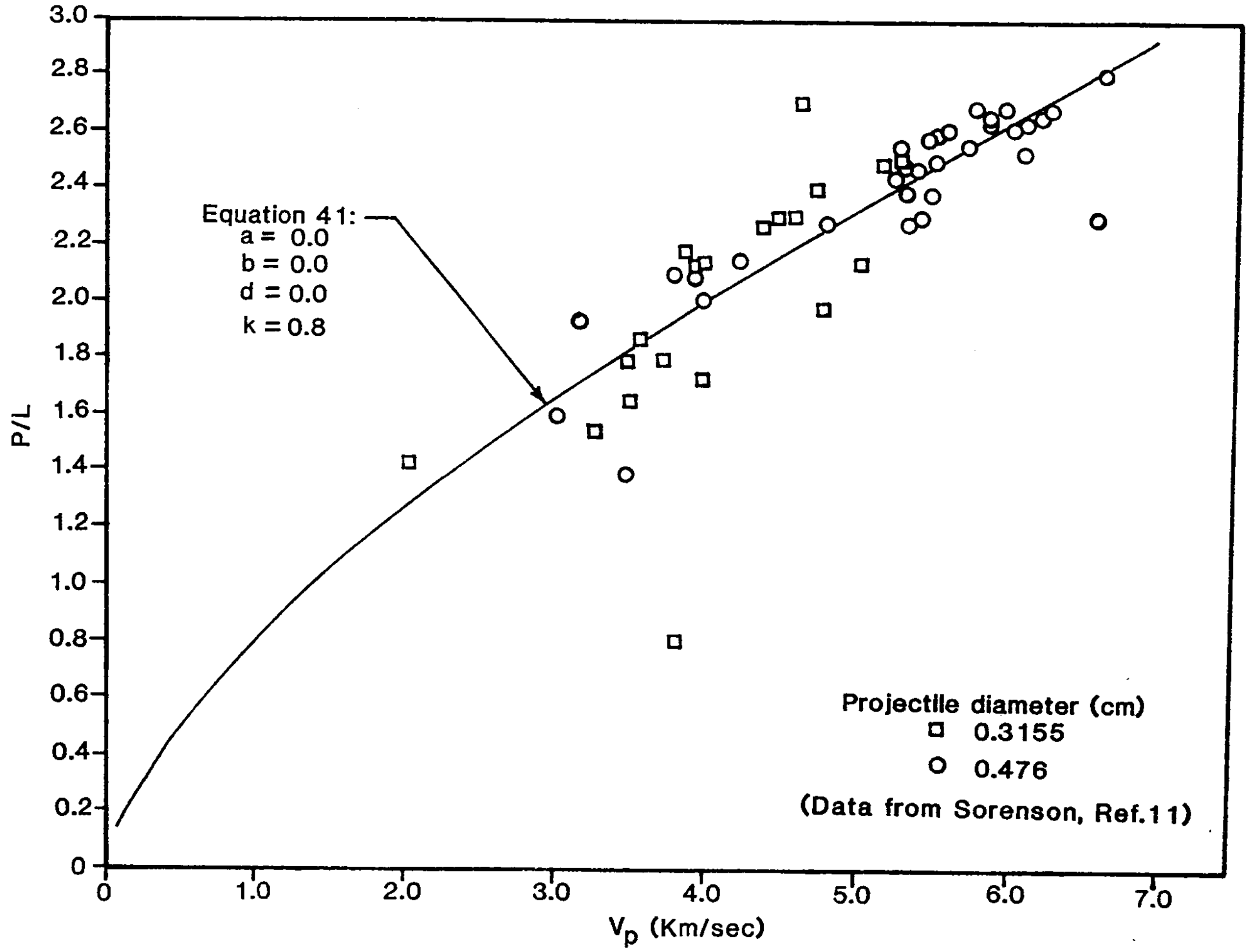

Figure 26. Penetration Curve of Aluminum Projectiles Impacting Semi-infinite Pure Aluminum Targets Calculated by Equation (41)

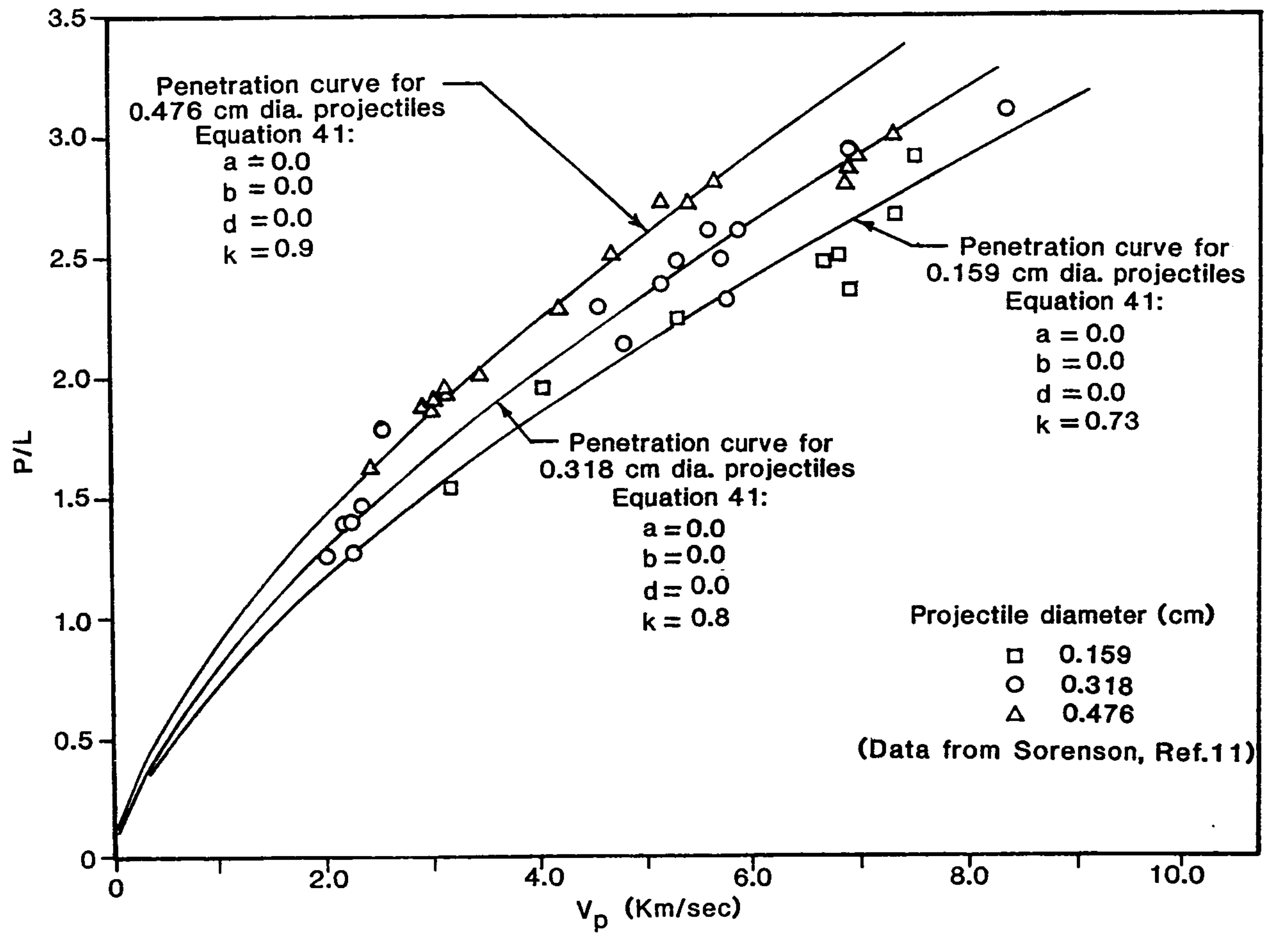

Figure 27. Penetration Curves for Aluminum Projectiles of Varying Diameter Impacting Semi-infinite Aluminum Targets Calculated by Equation (41)

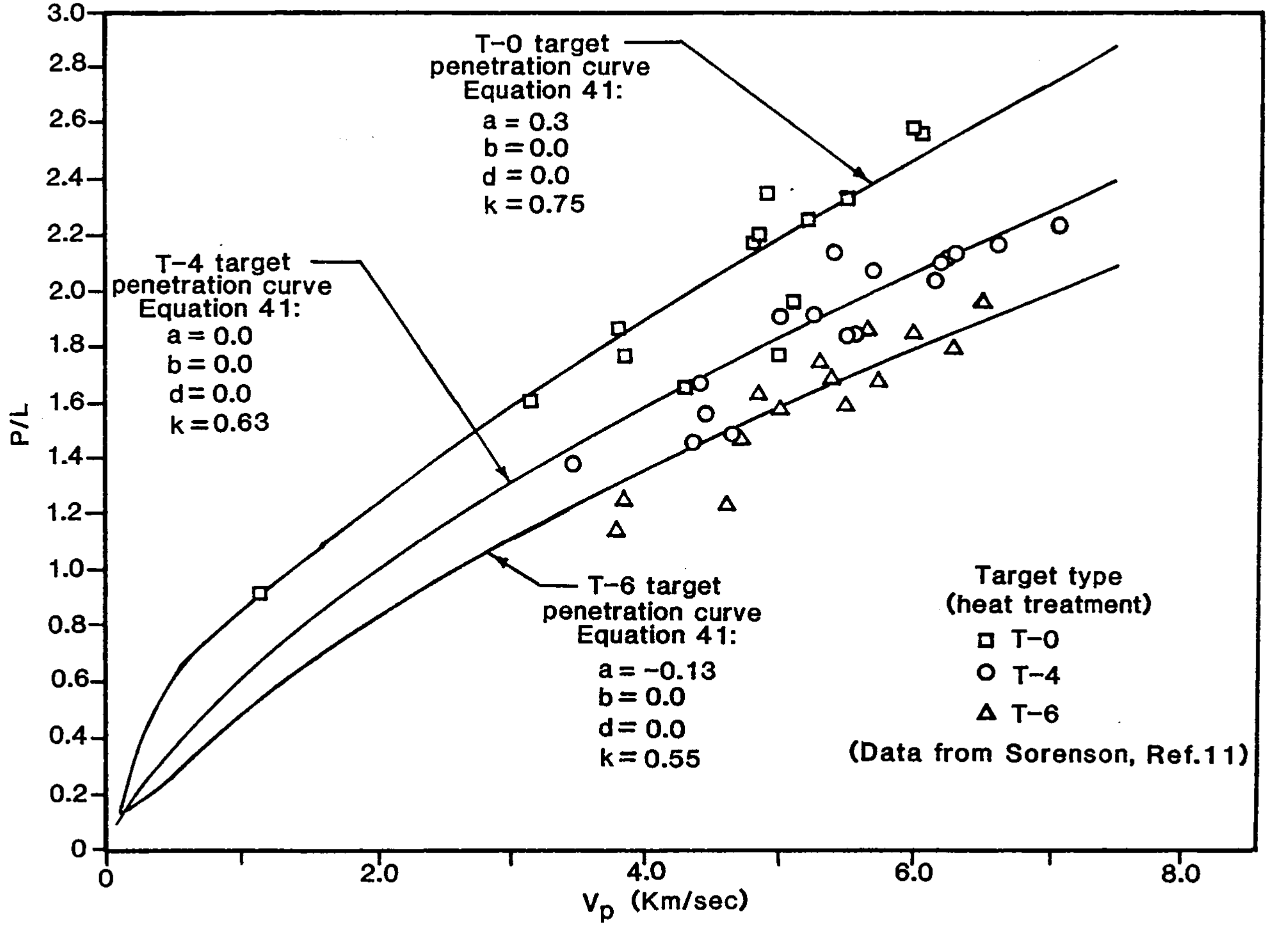

Figure 28. Penetration Curves for Aluminum Projectiles Impacting Semi-infinite Aluminum (6061) Targets of Varying Strengths Calculated by Equation (41)

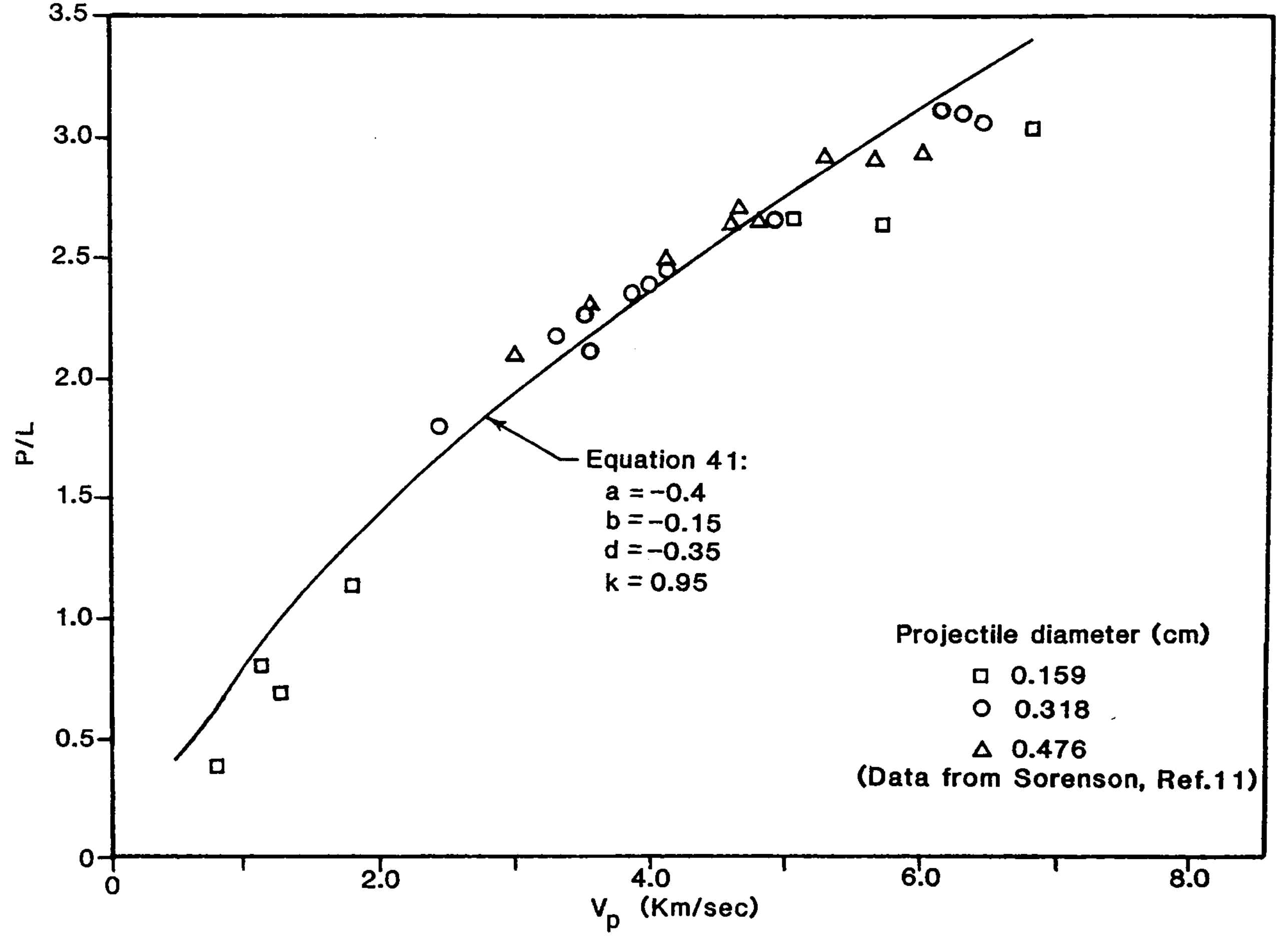

Figure 29. Penetration Curve of Copper Projectiles Impacting Semi-infinite Copper Targets Calculated by Equation (41)

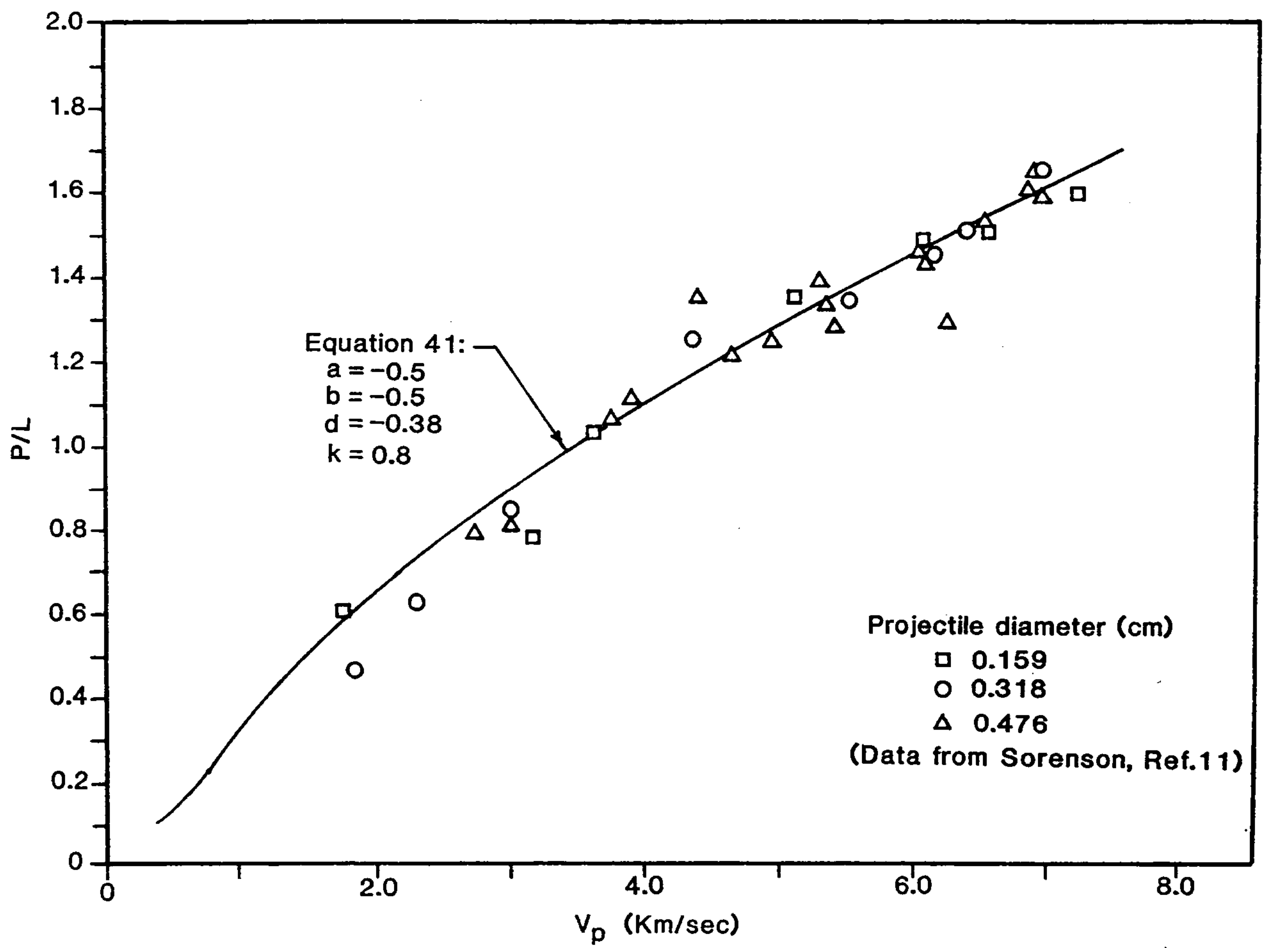

Figure 30. Penetration Curve of Aluminum Projectiles Impacting Semi-infinite Copper Targets Calculated by Equation (41)

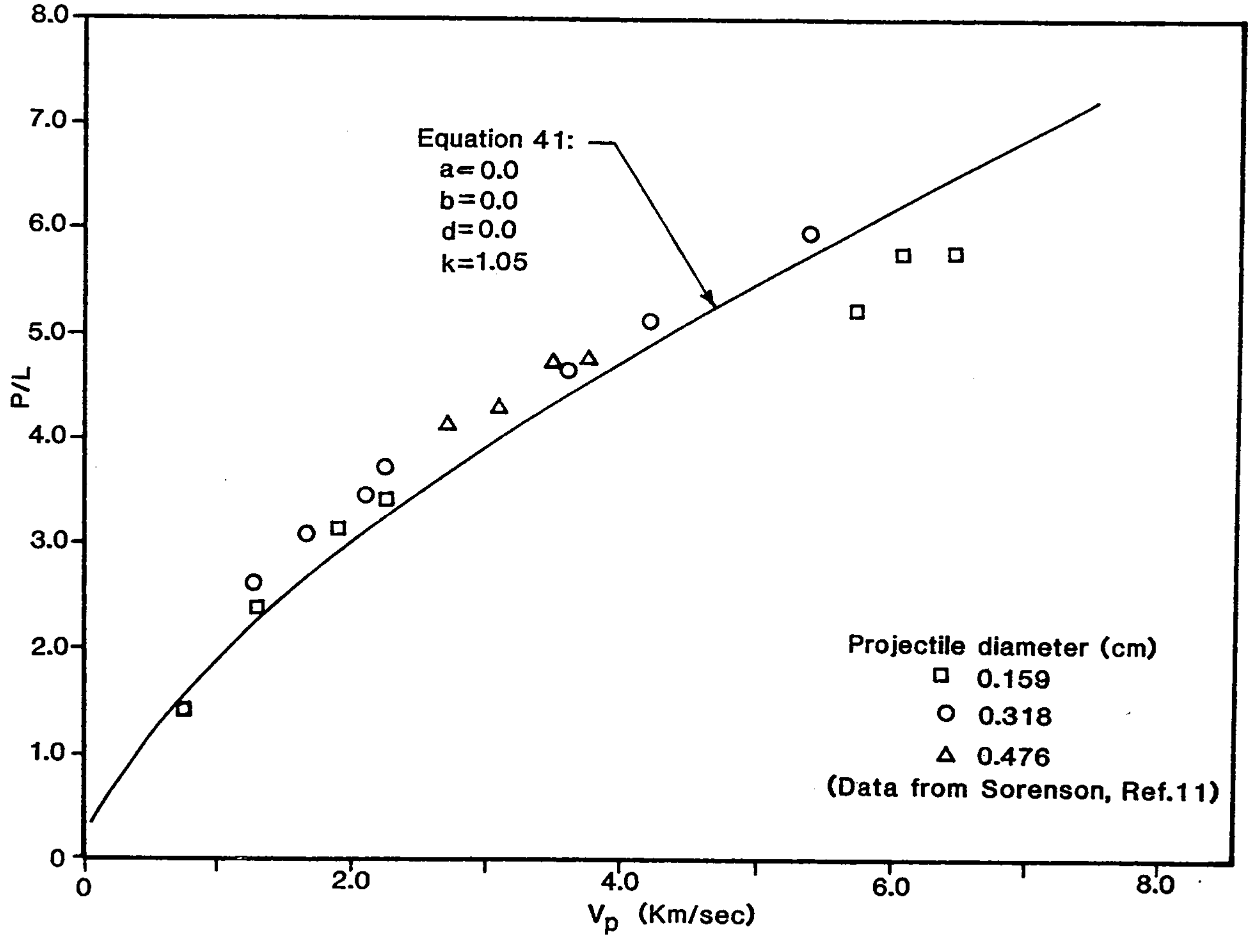

Figure 31. Penetration Curve of Copper Projectiles Impacting Semi-infinite Aluminum Targets Calculated by Equation (41)

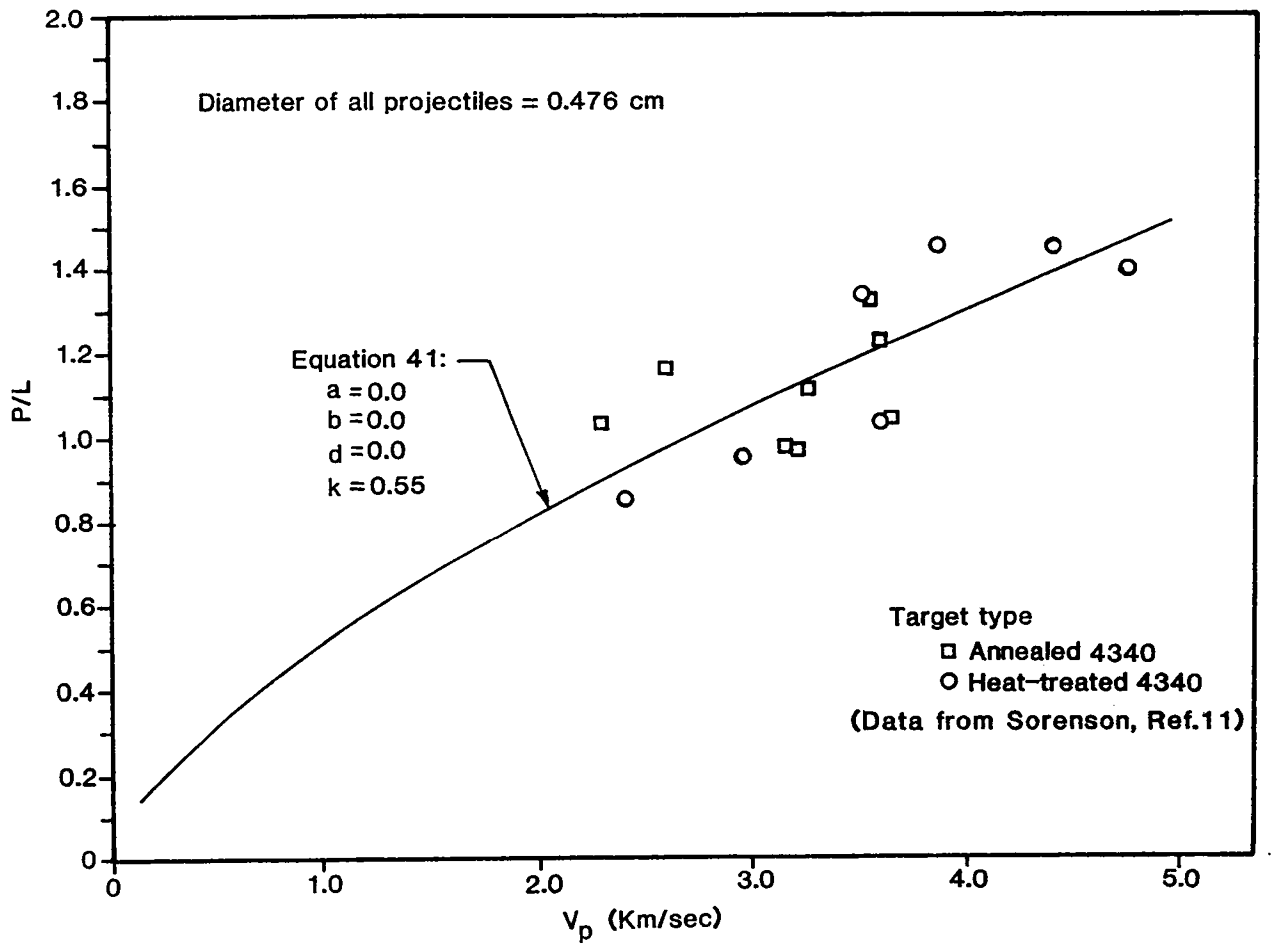

Figure 32. Penetration Curve of Steel Projectiles Impacting Semi-infinite Steel Targets Calculated by Equation (41)

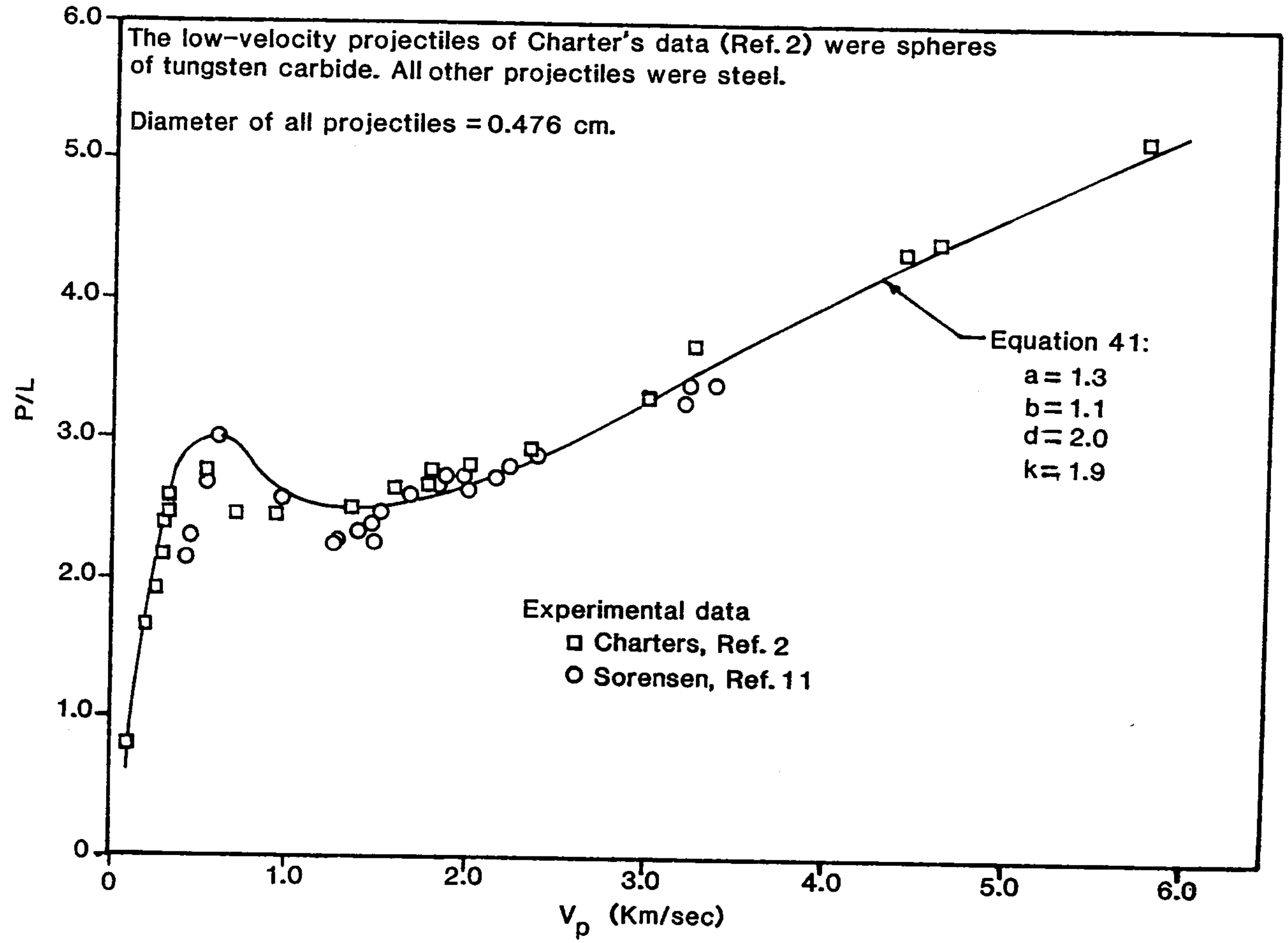

Figure 33. Penetration Curve of Steel Projectiles Impacting Semi-infinite Lead Targets Calculated by Equation (41)

APPENDIX B

TABLES

Table 1. Material Properties

Material	Density (g/cm^3)	Shear Strength ($dyne/cm^2$)
Aluminum		
Pure	2.699	6.58×10^8
6061-T0	2.7	8.69×10^8
6061-T4	2.7	1.66×10^9
6061-T6	2.7	2.18×10^9
Copper	8.77	1.385×10^9
Steel (4340)		
Annealed	7.85	5.52×10^9
Heat Treated	7.85	9.37×10^9
Lead	11.35	1.3×10^8
Celotex®	0.25	N/A
Bee's Wax	0.898	N/A

Table 2. Ammunition Description

Manufacturer	Description	Configuration	Length (mm)	Muzzle Velocity[A] (km/sec)	Projectile Mass (gm)
CCI	CB Short	1	9.4	0.22	1.97
Federal	Short	1	8.94	0.33	1.83
CCI	Short	2	9.27	0.35	1.72
Federal	Lightening	1	12.1	0.38	2.55
CCI	Blazer	1	12.2	0.38	2.57
CCI	Mini Mag	2	11.5	0.39	2.34
Winchester	Long Rifle	2	11.2	0.39	2.48
Remington	Viper	3	11.8	0.43	2.33
CCI	Stinger	2	10.2	0.50	1.98
CCI	Maxi Mag	2	10.6	0.58	2.42
CCI	Maxi Mag	1	11.0	0.58	2.49
Modified CCI	Maxi Mag	2	10.6	~0.58	~2.2
Modified CCI	Maxi Mag	1	11.0	~0.58	~2.2
Winchester	.223	5	18.0	1.01	3.43
Remington	.223	4	18.0	0.99	3.61
Modified Winchester	.223	5	18.0	~1.01	~3.3
Modified Remington	.223	4	18.0	~0.99	~3.5
Remington	Accelerator	4	17.0	1.24	3.58

[A] Velocities are quoted from References [14], [15], and [16].

Table 3. Lead Sphere Impacts into Semi-infinite Lead Targets

Projectile Diameter, D = 0.476 cm

Projectile Mass (mg)	Impact Velocity (Km/sec)	Crater Volume (cm^3)	Penetration Depth (cm)	P/L
635	0.41	0.29	0.518	1.09
630	0.56	0.61	0.668	1.40
638	0.63	0.83	0.790	1.66
636	0.74	1.11	0.844	1.77
637	0.83	1.15	0.854	1.79
634	0.84	1.42	0.930	1.95
637	0.85	1.41	0.905	1.90
645	0.86	1.37	0.894	1.88
638	0.86	1.30	0.879	1.85
636	0.88	1.39	0.935	1.96
634	1.05	1.37	0.905	1.90
638	1.09	1.52	0.970	2.04
642	1.10	2.10	1.040	2.18
639	1.23	2.25	1.1	2.31
639	1.29	1.45	0.960	2.02
639	1.30	2.77	1.172	2.46
628	1.35	2.92	1.188	2.50
638	1.37	3.02	1.229	2.58
641	1.38	2.78	1.168	2.45
637	1.41	3.62	1.218	2.56
620	1.45	3.08	1.201	2.52
638	1.56	3.05	1.165	2.45
638	1.68	4.18	1.325	2.78
641	1.71	5.20	1.53	3.21
639	1.83	4.42	1.302	2.74
638	1.99	4.42	1.290	2.71
638	2.02	5.06	1.432	3.01
659	2.09	5.18	1.41	2.96

Table 4. Aluminum Sphere Impacts into Semi-infinite Pure Aluminum Targets

A. Projectile Diameter, D = 0.476 cm

Impact Velocity (Km/sec)	Crater Volume (cm^3)	Penetration Depth (cm)	P/L
3.00	0.70	0.764	1.61
3.17	1.20	0.925	1.94
3.43	0.61	0.668	1.40
3.76	1.66	1.006	2.11
3.90	1.56	1.000	2.10
3.97	1.81	0.955	2.01
4.19	1.82	1.030	2.16
4.60	2.07	1.062	2.23
4.76	1.71	1.088	2.29
5.46	2.35	1.140	2.39
5.71	2.86	1.220	2.56
6.00	3.27	1.252	2.63
6.07	3.12	1.207	2.54
6.27	3.42	1.282	2.69

B. Projectile Diameter, D = 0.3155 cm

Impact Velocity (Km/sec)	Crater Volume (cm^3)	Penetration Depth (cm)	P/L
2.03	0.14	0.455	1.45
3.28	0.26	0.491	1.56
3.47	0.24	0.566	1.80
3.48	0.26	0.522	1.66
3.58	0.35	0.592	1.88
3.70	0.29	0.569	1.81
3.78	0.34	0.256	0.81
3.88	0.51	0.690	2.19
3.93	0.52	0.673	2.14
3.97	0.33	0.547	1.74
3.97	0.49	0.675	2.15

Table 4. Concluded

B. Concluded

Impact Velocity (Km/sec)	Crater Volume (cm^3)	Penetration Depth (cm)	P/L
4.37	0.54	0.718	2.28
4.48	0.67	0.731	2.32
4.57	0.68	0.731	2.32
4.61	0.82	0.856	2.72
4.71	0.74	0.759	2.41
4.72	0.50	0.626	1.99
4.99	0.56	0.675	2.15
5.18	0.82	0.786	2.50
5.24	0.82	0.793	2.52
5.24	0.85	0.774	2.46
5.27	0.93	0.806	2.56
5.29	0.73	0.754	2.40
5.29	0.86	0.779	2.48
5.34	0.65	0.720	2.29
5.36	0.81	0.780	2.48
5.38	0.70	0.724	2.30
5.44	0.91	0.813	2.59
5.49	0.87	0.790	2.51
5.53	0.91	0.823	2.61
5.56	0.96	0.824	2.62
5.74	0.94	0.850	2.70
5.85	1.00	0.838	2.66
5.86	1.02	0.832	2.65
5.93	1.05	0.848	2.70
6.09	1.00	0.834	2.65
6.19	1.10	0.839	2.67
6.53	0.69	0.730	2.32
6.61	1.21	0.886	2.82

Table 5. Aluminum Sphere Impacts into Semi-infinite Aluminum Targets

A. Projectile Diameter, D = 0.159 cm

Impact Velocity (Km/sec)	Crater Volume (cm^3)	Penetration Depth (cm)	P/L
3.200	0.053	0.245	1.54
4.076	0.074	0.310	1.95
5.322	0.091	0.354	2.23
6.654	0.142	0.392	2.47
6.793	0.142	0.398	2.50
6.924	0.133	0.373	2.35
7.292	0.155	0.425	2.67
7.507	0.168	0.462	2.91

B. Projectile Diameter, D = 0.318 cm

Impact Velocity (Km/sec)	Crater Volume (cm^3)	Penetration Depth (cm)	P/L
2.048	0.134	0.399	1.26
2.254	0.201	0.445	1.40
2.263	0.207	0.445	1.40
2.317	0.155	0.408	1.29
2.348	0.160	0.469	1.48
2.548	0.365	0.570	1.80
4.549	0.775	0.730	2.30
4.820	0.661	0.678	2.14
5.148	0.869	0.758	2.39
5.289	0.729	0.789	2.49
5.612	1.074	0.829	2.61
5.694	0.929	0.790	2.49
5.751	0.819	0.737	2.32
5.881	1.180	0.828	2.61
6.920	1.430	0.936	2.95
8.367	2.081	0.990	3.12

Table 5. Concluded

C. Projectile Diameter, D = 0.476 cm

Impact Velocity (Km/sec)	Crater Volume (cm^3)	Penetration Depth (cm)	P/L
2.548	0.929	0.799	1.68
2.977	1.313	0.895	1.88
3.024	1.308	0.898	1.89
3.049	1.352	0.905	1.90
3.107	1.387	0.902	1.89
3.131	1.406	0.926	1.94
3.146	1.410	0.913	1.92
3.447	1.583	0.951	2.00
4.223	2.272	1.088	2.28
4.727	2.867	1.194	2.51
5.166	3.476	1.298	2.73
5.404	3.589	1.296	2.72
5.632	4.519	1.337	2.81
6.884	4.671	1.363	2.86
6.876	4.135	1.334	2.80
6.925	4.789	1.392	2.92
7.306	5.202	1.429	3.00

Table 6. Aluminum Sphere Impacts into Semi-infinite Aluminum (6061) Targets

A. T-0 Condition

Projectile Diameter (cm)	Impact Velocity (Km/sec)	Crater Volume (cm^3)	Penetration Depth (cm)	P/L
0.318	1.13	0.052	0.297	0.935
0.318	3.14	0.21	0.516	1.62
0.318	3.82	0.38	0.597	1.88
0.318	3.84	0.33	0.564	1.78
0.318	4.30	0.30	0.529	1.67
0.318	4.85	0.61	0.706	2.22
0.476	4.85	1.89	1.041	2.19
0.318	4.91	0.55	0.754	2.37
0.318	5.00	0.32	0.569	1.79
0.318	5.10	0.68	0.630	1.98
0.318	5.20	0.66	0.721	2.27
0.318	5.50	0.70	0.747	2.35
0.318	6.60	0.97	0.826	2.60
0.318	6.60	0.76	0.818	2.58

B. T-4 Condition

Projectile Diameter (cm)	Impact Velocity (Km/sec)	Crater Volume (cm^3)	Penetration Depth (cm)	P/L
0.318	3.44	0.20	0.442	1.39
0.318	4.3	0.21	0.467	1.47
0.476	4.4	0.85	0.798	1.68
0.476	4.4	0.76	0.747	1.57
0.476	4.65	0.69	0.714	1.50
0.318	5.0	0.42	0.610	1.92
0.318	5.25	0.45	0.612	1.93
0.318	5.40	0.45	0.683	2.15
0.318	5.50	0.38	0.586	1.85

Table 6. Concluded

B. Concluded

Projectile Diameter (cm)	Impact Velocity (Km/sec)	Crater Volume (cm^3)	Penetration Depth (cm)	P/L
0.318	3.48	0.15	0.394	1.24
0.318	3.82	0.12	0.366	1.15
0.318	3.86	0.15	0.401	1.26
0.318	4.60	0.13	0.394	1.24
0.318	4.70	0.22	0.470	1.48
0.318	4.88	0.27	0.523	1.65
0.476	5.00	0.98	0.759	1.59
0.318	5.30	0.38	0.556	1.75
0.318	5.40	0.32	0.541	1.70
0.318	5.50	0.32	0.508	1.60
0.476	5.65	1.09	0.889	1.87
0.476	5.75	1.05	0.803	1.69
0.318	6.00	0.43	0.589	1.86
0.318	6.30	0.40	0.571	1.80
0.318	6.50	0.52	0.625	1.97

C. T-6 Condition

Projectile Diameter (cm)	Impact Velocity (Km/sec)	Crater Volume (cm^3)	Penetration Depth (cm)	P/L
0.318	5.65	0.44	0.594	1.87
0.318	5.65	0.40	0.592	1.86
0.476	5.70	1.71	0.996	2.09
0.318	6.13	0.52	0.650	2.05
0.318	6.20	0.57	0.670	2.11
0.318	6.20	0.56	0.681	2.14
0.318	6.30	0.57	0.683	2.15
0.318	6.60	0.63	0.693	2.18
0.476	7.05	2.02	1.072	2.25

Table 7. Copper Sphere Impacts into Semi-infinite Copper Targets

A. Projectile Diameter, D = 0.159 cm

Impact Velocity (Km/sec)	Crater Volume (cm^3)	Penetration Depth (cm)	P/L
0.806	0.006	0.061	0.384
1.146	0.009	0.128	0.805
1.289	0.008	0.109	0.69
1.798	0.018	1.182	1.14
5.038	0.143	0.425	2.67
5.716	0.146	0.419	2.64
6.775	0.208	0.484	3.04
7.574	0.280	0.526	3.31

B. Projectile Diameter, D = 0.318 cm

Impact Velocity (Km/sec)	Crater Volume (cm^3)	Penetration Depth (cm)	P/L
2.448	0.344	0.573	1.80
3.287	0.537	0.688	2.17
3.518	0.611	0.717	2.26
3.582	0.572	0.671	2.11
3.833	0.688	0.749	2.36
3.978	0.723	0.758	2.39
4.088	0.772	0.778	2.45
4.908	1.074	0.843	2.66
6.146	1.440	0.987	3.11
6.305	1.570	0.984	3.10
6.440	1.630	0.972	3.06

Table 7. Concluded

C. Projectile Diameter, D=0.476 cm

Impact Velocity (Km/sec)	Crater Volume (cm^3)	Penetration Depth (cm)	P/L
2.926	1.608	0.996	2.09
3.520	2.124	1.093	2.30
4.038	2.701	1.184	2.49
4.538	3.191	1.256	2.64
4.605	3.330	1.292	2.71
4.736	3.501	1.260	2.65
5.270	4.161	1.391	2.92
5.586	4.422	1.387	2.91
5.967	4.822	1.395	2.93

Table 8. Aluminum Sphere Impacts into Semi-infinite Copper Targets

A. Projectile Diameter, D = 0.159 cm

Impact Velocity (Km/sec)	Crater Volume (cm^3)	Penetration Depth (cm)	P/L
1.748	0.007	0.097	0.611
3.134	0.015	0.124	0.781
3.603	0.017	0.163	1.03
5.106	0.034	0.214	1.35
6.020	0.034	0.237	1.49
6.106	0.039	0.229	1.44
6.539	0.044	0.240	1.51
7.205	0.046	0.254	1.60
7.574	0.059	0.249	1.57
8.819	0.069	0.318	2.00

B. Projectile Diameter, D = 0.318 cm

Impact Velocity (Km/sec)	Crater Volume (cm^3)	Penetration Depth (cm)	P/L
1.833	0.037	0.149	0.469
2.324	0.074	0.199	0.627
2.990	0.089	0.269	0.847
4.357	0.177	0.396	1.25
5.514	0.231	0.426	1.34
6.141	0.261	0.461	1.45
6.944	0.374	0.525	1.65
6.400	0.310	0.478	1.51

Table 8. Concluded

C. Projectile Diameter, D=0.476 cm

Impact Velocity (Km/sec)	Crater Volume (cm^3)	Penetration Depth (cm)	P/L
2.697	0.251	0.374	0.786
2.973	0.290	0.384	0.807
3.729	0.410	0.503	1.06
3.914	0.438	0.528	1.11
4.396	0.698	0.641	1.35
4.645	0.575	0.574	1.21
4.969	0.656	0.591	1.24
5.309	0.809	0.662	1.39
5.328	0.751	0.635	1.33
5.377	0.684	0.609	1.28
6.022	0.951	0.693	1.46
6.106	0.880	0.682	1.43
6.262	0.710	0.613	1.29
6.563	1.031	0.722	1.52
6.868	1.010	0.766	1.61
6.896	1.219	0.784	1.65
6.950	1.141	0.755	1.59

Table 9. Copper Sphere Impacts into Semi-infinite Aluminum Targets

A. Projectile Diameter, D = 0.159 cm

Impact Velocity (Km/sec)	Crater Volume (cm^3)	Penetration Depth (cm)	P/L
0.772	0.010	0.229	1.44
1.313	0.030	0.380	2.39
1.912	0.069	0.500	3.15
2.276	0.103	0.546	3.44
5.687	0.565	0.833	5.25
6.090	0.610	0.917	5.78
6.436	0.679	0.917	5.78

B. Projectile Diameter, D = 0.318 cm

Impact Velocity (Km/sec)	Crater Volume (cm^3)	Penetration Depth (cm)	P/L
1.278	0.270	0.833	2.62
1.678	0.531	0.988	3.11
2.133	1.003	1.097	3.46
2.240	1.023	1.185	3.73
3.604	2.560	1.476	4.65
4.206	3.401	1.631	5.14
5.340	4.851	1.897	5.97

C. Projectile Diameter, D = 0.476 cm

Impact Velocity (Km/sec)	Crater Volume (cm^3)	Penetration Depth (cm)	P/L
2.690	5.212	1.966	4.13
3.086	6.363	2.047	4.30
3.496	8.143	2.258	4.74
3.741	9.042	2.276	4.78

Table 10. Steel Sphere Impacts into Semi-infinite Steel (4340) Targets

Projectile Diameter = 0.476 cm

A. Annealed Targets

Impact Velocity (Km/sec)	Crater Volume (cm^3)	Penetration Depth (cm)	P/L
2.30	0.27	0.493	1.035
2.58	0.37	0.554	1.162
3.14	0.39	0.464	0.975
3.21	0.21	0.463	0.971
3.27	0.40	0.539	1.113
3.53	0.45	0.630	1.325
3.57	0.40	0.583	1.225
3.60	0.30	0.498	1.048

B. Heat-Treated Targets

Impact Velocity (Km/sec)	Crater Volume (cm^3)	Penetration Depth (cm)	P/L
2.38	0.16	0.406	0.853
2.89	0.24	0.449	0.953
3.52	0.35	0.638	1.338
3.60	0.21	0.493	1.035
3.84	0.39	0.694	1.455
4.40	0.39	0.661	1.387
4.75	0.42	0.666	1.400

Table 11. Steel Sphere Impacts into Semi-infinite Lead Targets

Impact Velocity (Km/sec)	Crater Volume (cm^3)	Penetration Depth (cm)	P/L
0.44	0.30	1.03	2.16
0.47	0.35	1.11	2.33
0.56	0.48	1.29	2.71
0.63	0.60	1.44	3.02
0.98	1.07	1.23	2.58
1.28	1.77	1.08	2.27
1.30	1.85	1.09	2.29
1.40	2.13	1.12	2.35
1.48	2.41	1.15	2.42
1.49	2.35	1.09	2.29
1.51	2.33	1.16	2.435
1.53	2.45	1.19	2.50
1.66	2.70	1.26	2.64
1.69	2.82	1.25	2.62
1.83	3.16	1.29	2.71
1.88	3.47	1.32	2.78
1.99	3.60	1.32	2.78
2.02	3.88	1.27	2.67
2.17	4.05	1.31	2.75
2.24	4.40	1.35	2.84
2.38	4.70	1.41	2.96
2.42	4.25	1.40	2.93
3.21	7.21	1.57	3.3
3.24	7.54	1.63	3.41
3.4	7.90	1.63	3.41

VITA

Raymond P. Young, Jr. was born in Manchester, Tennessee on November 18, 1959. He attended elementary schools in Manchester and graduated from Coffee County Central High School in June 1978. The following four years of study were spent at Tennessee Technological University, from which he earned a B. S. in Mechanical Engineering in 1982. He has worked since then with Calspan Corporation/AEDC Division at the Arnold Engineering Development Center, Arnold Air Force Base, Tennessee. Concurrently, he studied at The University of Tennessee Space Institute and received a Master of Science Degree in Mechanical Engineering in December 1991.